

LETTER TO THE EDITOR

# Galactic Mass-to-Light Ratios With Superfluid Dark Matter

T. Mistele<sup>1</sup>, S. McGaugh<sup>2</sup>, and S. Hossenfelder<sup>1</sup>

<sup>1</sup> Frankfurt Institute for Advanced Studies, Ruth-Moufang-Str. 1, D 60438 Frankfurt am Main, Germany  
e-mail: mistele@fias.uni-frankfurt.de

<sup>2</sup> Department of Astronomy, Case Western Reserve University, 10900 Euclid Avenue, Cleveland, OH 44106, USA

January 20, 2022

## ABSTRACT

*Context.* We make rotation curve fits to test the superfluid dark matter model.

*Aims.* Our aim is to investigate whether superfluid dark matter provides satisfactory fits to galactic rotation curves with reasonable stellar mass-to-light ratios.

*Methods.* We fitted the superfluid dark matter model to the rotation curves of 169 galaxies in the SPARC sample.

*Results.* We found that the mass-to-light ratios obtained with superfluid dark matter are generally acceptable in terms of stellar populations. However, the best fit mass-to-light ratios have an unnatural dependence on the size of the galaxy in that giant galaxies have systematically lower mass-to-light ratios than dwarf galaxies. A second finding is that the superfluid often fits the rotation curves best when the superfluid's force does not closely resemble that of Modified Newtonian Dynamics (MOND). In that case, we can no longer expect superfluid dark matter to reproduce the phenomenologically observed scaling-relations that make MOND appealing. If, on the other hand, we consider only solutions whose force approximates MOND well, then the total mass of the superfluid is in tension with gravitational lensing data.

*Conclusions.* We conclude that even the best fits with superfluid dark matter are still unsatisfactory.

**Key words.** galactic rotation curves – cold dark matter – modified gravity – strong gravitational lensing

## 1. Introduction

In 2015, Berezhiani & Khoury proposed a new hypothesis that combines features of Cold Dark Matter (CDM) and Modified Newtonian Dynamics (MOND) (Milgrom 1983b,a,c; Bekenstein & Milgrom 1984): superfluid dark matter, hereafter SFDM. In SFDM, dark matter is composed of a light ( $\sim$ eV) scalar field which can condense to a superfluid. In the superfluid phase, phonons mediate a force which is similar to the force of MOND. This hypothesis has since passed several observational tests (Berezhiani et al. 2018; Hossenfelder & Mistele 2019, 2020).

However, recently it was found that SFDM needs about 20% less baryonic mass than MOND to fit the Milky Way rotation curve at  $R \lesssim 25$  kpc (Hossenfelder & Mistele 2020). To investigate whether this is a general trend, we fit SFDM to the SPARC data (Lelli et al. 2016) with the stellar mass-to-light ratio  $M/L_*$  as a fitting parameter.

## 2. Models

SFDM requires four parameters for which we use the fiducial values from Berezhiani et al. (2018),  $m = 1$  eV,  $\Lambda = 0.05$  meV,  $\alpha = 5.7$ , and  $\beta = 2$ . We keep those parameters fixed, see also Appendix D.2.6.

The total acceleration inside the superfluid core of a galaxy is  $\mathbf{a}_{\text{tot}} = \mathbf{a}_\theta + \mathbf{a}_b + \mathbf{a}_{\text{SF}}$ , where  $\mathbf{a}_\theta$  is the acceleration created by the phonon force,  $\mathbf{a}_{\text{SF}}$  the acceleration stemming from the normal gravitational attraction of the superfluid, and  $\mathbf{a}_b$  that stemming from the mass of the baryons. The position-dependence of those accelerations is determined by the SFDM equations of motion and the distribution of baryonic mass. At a transition radius

where the superfluid condensate is estimated to break down, one matches the superfluid core to an NFW halo (Berezhiani et al. 2018). We assume that all rotation curve data points are within the superfluid core; otherwise rotation curves will not be naturally MOND-like.

From integrating the standard Poisson equation including the superfluid's energy density  $\rho_{\text{SF}}$  as a source term, one obtains  $\hat{\mu}(\mathbf{x}) = \mu_{\text{nr}} - m\phi_N(\mathbf{x})$ , where  $\mu_{\text{nr}}$  is the chemical potential and  $\phi_N(\mathbf{x})$  is the Newtonian gravitational potential. The gradient of  $\phi_N(\mathbf{x})$  gives  $\mathbf{a}_b + \mathbf{a}_{\text{SF}}$ . In the so-called no-curl approximation, one obtains the phonon force  $\mathbf{a}_\theta$  as an algebraic function of  $\mathbf{a}_b$  and  $\varepsilon_*(\mathbf{x})$  (see Appendix A.1),

$$\varepsilon_*(\mathbf{x}) := \frac{2m^2}{\alpha M_{\text{Pl}} |\mathbf{a}_b(\mathbf{x})|} \frac{\hat{\mu}(\mathbf{x})}{m}, \quad (1)$$

where  $M_{\text{Pl}}$  is the Planck mass (it enters through Newton's constant). The quantity  $\varepsilon_*(\mathbf{x})$  controls how closely SFDM resembles MOND. We will refer to  $|\varepsilon_*| \ll 1$  as the MOND-limit and to  $|\varepsilon_*| = \mathcal{O}(1)$  as the pseudo-MOND limit. The relation between  $\varepsilon_*$  and these limits of SFDM was previously derived in Mistele (2021). Details on the definition and rationale behind these limits are in Appendix A.

Solutions of the equations of motion can be parameterized by one boundary condition,  $\varepsilon := \varepsilon_*(R_{\text{mid}})$ , where  $R_{\text{mid}} := (R_{\text{min}} + R_{\text{max}})/2$ , and  $R_{\text{min}}$  ( $R_{\text{max}}$ ) is the smallest (largest) radius with a rotation curve data point.  $\varepsilon$  quantifies how closely the phonon force resembles a MOND-force in the middle of the observed rotation curve.

We will compare SFDM to MOND with one of the standard interpolation functions (Lelli et al. 2017)

$$v_e(y) = \frac{1}{1 - e^{-\sqrt{y}}}, \quad (2)$$

where  $y = |a_b|/a_0$  and  $a_0$  is the one free parameter in MOND. In SFDM the interpolation function is slower to reach its limits for large and small  $y$ . Also, usually  $a_0$  is chosen smaller in SFDM compared to MOND to account for the presence of  $a_{\text{SF}}$  (Berezhiani et al. 2018). For MOND, we adopt  $a_0^{\text{MOND}} \approx 1.2 \cdot 10^{-10} \text{ m/s}^2$  from Lelli et al. (2017). For SFDM, the fiducial parameters from Berezhiani et al. (2018) give  $a_0^{\text{SFDM}} \approx 0.87 \cdot 10^{-10} \text{ m/s}^2$ .

To check how sensitive our results are to the particular theoretical realization of SFDM we include the two-field model from Mistele (2021). In this two-field model, the phenomenology on galactic scales is similar to standard SFDM, but it has the advantages that (a) it does not require ad-hoc finite-temperature corrections for stability, (b) its phonon force is always close to its MOND-limit, and (c) the superfluid can remain in equilibrium much longer than galactic timescales. Both models are described in more detail in Appendix A.

### 3. Data

We take the observed rotation velocity  $V_{\text{obs}}$  directly from SPARC (Lelli et al. 2016). To find the best SFDM fit, we then need the baryonic energy density  $\rho_b(R, z)$  because it is a source for the equation of motion of the superfluid. For this, we use updated high-resolution mass models including resolved gas surface density profiles for 169 of the 175 SPARC galaxies (Lelli 2021, private communication). We exclude the 6 galaxies lacking radial profiles for the gas distribution.

These mass models provide surface densities  $\Sigma$  for the bulge, the stellar disk, and the HI disk of each galaxy for a discrete set of positions. We linearly interpolate the data points and assume constant density at radii smaller than the smallest radius in the series, and zero density at radii larger than the largest radius in the series. This gives a simple, data-compatible approximation for the density distribution at all radii.

For the bulge, we assume spherical symmetry and extract its energy density from its surface density by an Abel transform

$$\rho_{\text{bulge}}(r) = -\frac{1}{\pi} \int_0^\infty d\bar{r} \frac{\Sigma'_{\text{bulge}}(\sqrt{\bar{r}^2 + r^2})}{\sqrt{\bar{r}^2 + r^2}}. \quad (3)$$

For the stellar disk, we assume a scale height  $h_*$  (Lelli et al. 2016)

$$h_* = 0.196 \cdot (R_{\text{disk}}[\text{kpc}])^{0.633} \text{ kpc}, \quad (4)$$

where  $R_{\text{disk}}$  is the disk scale length from SPARC. Again, we use a linear interpolation of the SPARC surface brightness data points.

For the gas disk we do the same as for the stellar disk, except that in this case we assume a fixed scale height  $h_g = 0.130 \text{ kpc}$ . This is the same scale height used in Hossfelder & Mistele (2020). We do not expect this choice of scale height to significantly affect the results. To account for the non-HI gas, we multiply the HI surface density by 1.4 (McGaugh et al. 2020).

### 4. Method

In our fitting procedure, we keep  $V_{\text{obs}}$  and the fiducial model parameters of SFDM fixed, but we allow a common factor  $Q_*$  to

adjust the stellar disk and bulge  $M/L_*$  relative to  $(M/L_*)_{\text{disk}} = 0.5$  and  $(M/L_*)_{\text{bulge}} = 0.7$ ,

$$\begin{aligned} \rho_b(R, z) &= \rho_{\text{gas}}(R, z) + 0.5 \cdot Q_* \cdot \rho_*(R, z) \\ &+ 0.7 \cdot Q_* \cdot \rho_{\text{bulge}}(\sqrt{R^2 + z^2}). \end{aligned} \quad (5)$$

Using this total baryonic energy density, we solve the SFDM equations of motion for different boundary conditions. From that we then obtain the expected rotation curve.

In our fits, we require that  $\varepsilon_*(\mathbf{x})$  (see Eq. (1)) is larger than an algebraic minimum value  $\varepsilon_{\text{min}}$  everywhere within the superfluid. This minimum value is reached when  $\rho_{\text{SF}}$  vanishes and (for the case of  $\beta = 2$ ) is given by  $\varepsilon_{\text{min}} = -\sqrt{3/32} \approx -0.31$ . As mentioned in section 2, we parametrize solutions with  $\varepsilon = \varepsilon_*(R_{\text{mid}})$ .

After solving the SFDM equations of motion, we check whether all data points lie within the superfluid core. It turns out that for 31 of the 169 galaxies this is not the case. However, the criterion for the exact value of the transition-radius to the NFW halo is quite ad-hoc. We therefore do not discard these solutions, though we have checked that they do not alter the main conclusions, see also Appendix D.2.7.

Then we compare how good this rotation curve matches with the observed velocities,  $V_{\text{obs}}$ , from SPARC. For this, we define the best fit for each galaxy as that with the smallest  $\chi^2$ ,

$$\chi^2 = \frac{1}{N - f} \sum_R \frac{(V_{\text{obs}}(R) - V_c(R))^2}{\sigma_{V_{\text{obs}}}^2(R)}. \quad (6)$$

Here,  $N$  is the number of data points in the galaxy,  $f = 2$  is the number of fit parameters ( $Q_*$  and  $\varepsilon$ ),  $\sigma_{V_{\text{obs}}}$  is the uncertainty on the velocity  $V_{\text{obs}}$  from SPARC,  $V_c(R)$  is the calculated rotation curve in SFDM, and the sum is over the data points at radius  $R$ .

We minimize  $\chi^2$  for

$$10^{-2} \leq Q_* \leq 15, \quad (7)$$

$$10^{-2} \leq (\varepsilon - \varepsilon_{\text{min}}) \leq 10^4. \quad (8)$$

In our fit code, we scan values of  $\log_{10}(Q_*)$  and  $\log_{10}(\varepsilon - \varepsilon_{\text{min}})$ .

In the SPARC data, the Newtonian acceleration due to gas sometimes points outwards from the galactic center, not towards it, because of a hole in the HI data, possibly due to a transition from atomic to molecular gas. Usually, such a negative gas contribution is countered by the positive contributions from the stellar disk and the bulge and does not pose a problem. When this is not the case, there is technically no stable circular orbit so we cannot calculate a rotation curve. When this happens, we omit those data points when calculating  $\chi^2$ .

As a cross-check and as a comparison for SFDM, we also fit the radial acceleration relation (RAR) to the SPARC data, i.e. we fit the SPARC data with MOND assuming no curl term and the exponential interpolation function  $v_e$  (Lelli et al. 2017). In this case, we have only one free fit parameter,  $Q_*$ , and consequently, when calculating  $\chi^2$ , we set  $f = 1$ . We describe our fitting and calculation methods in more detail in Appendix C.

### 5. Results

The result of our MOND fit is similar to that of Li et al. (2018), which also fitted the RAR to SPARC galaxies. The major difference is that Li et al. (2018) used a MCMC procedure with Gaussian priors, while we used a simple parameter scan to minimize  $\chi^2$ . We also do not vary distance and inclination and do not separately vary the mass-to-light ratio of the stellar disk and the bulge. As a consequence of this simplified fitting procedure,

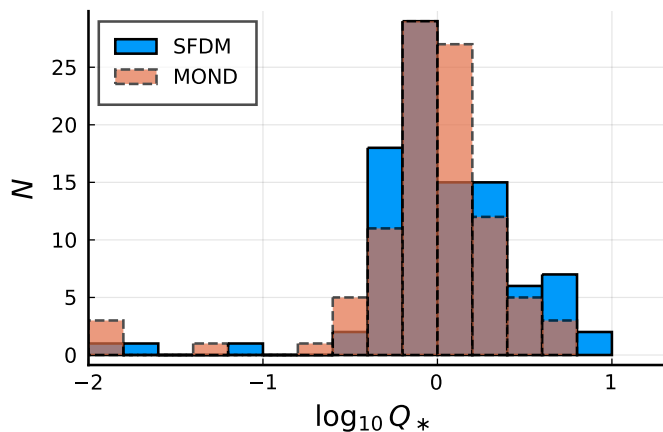


**Fig. 1.** Histograms of the best-fit  $Q_*$  values for the SFDM and MOND fits restricted to the  $Q = 1$  galaxies.

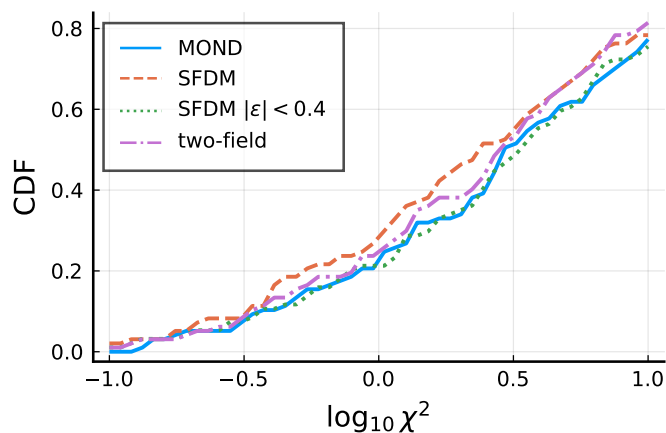


**Fig. 2.** Best-fit  $\chi^2$  cumulative distribution functions for the  $Q = 1$  galaxies for different models.

our distribution of best-fit  $M/L_*$  has more outliers and looks less Gaussian than that of Li et al. (2018).

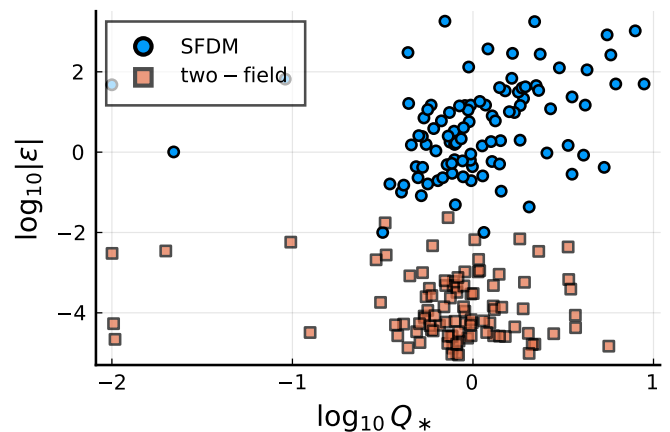
Still, our median best-fit stellar mass-to-light ratios and the best-fit  $\chi^2$  values are similar to those from Li et al. (2018). The median stellar disk  $M/L_*$  is 0.39. When we restrict ourselves to galaxies with high quality data ( $Q = 1$ ), this becomes 0.47, very similar to the 0.50 from Li et al. (2018). We show the  $\chi^2$  cumulative distribution function (CDF) in Fig. 2 which is also in reasonable agreement with Li et al. (2018).

In Fig. 1, one sees that some galaxies end up at the minimum stellar mass-to-light ratio allowed in our fitting method, corresponding to  $Q_* \approx 0.01$ . If we do not restrict ourselves to  $Q = 1$ , this peak at  $Q_* \approx 0.01$  is even more pronounced. As discussed in Appendix D.1, this is an artifact of our fitting procedure and can be ignored in what follows.

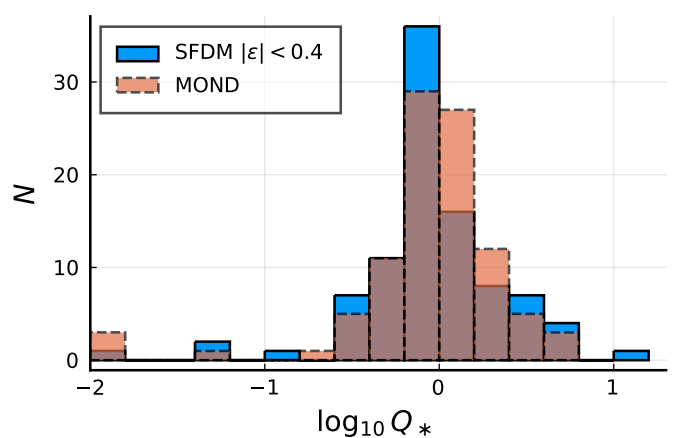
### 5.1. MOND vs SFDM

Fig. 1 shows the best-fit  $Q_*$  for the 97 galaxies with  $Q = 1$ . Contrary to what one might naively expect from the Milky Way result (Hossfelder & Mistele 2019), the SFDM fits do not have significantly smaller  $Q_*$  than the MOND fits. Indeed, the median  $Q_*$  for the  $Q = 1$  galaxies is about 4% larger than for MOND.

One reason for this is that for many galaxies the superfluid is not in the MOND-limit  $|\epsilon| \ll 1$ , as one sees from Fig. 3. We theoretically explain why going outside the MOND limit allows



**Fig. 3.** The best-fit  $\epsilon$  values versus the best-fit  $Q_*$  values for the  $Q = 1$  galaxies. For standard SFDM, the correlation coefficient is  $r = 0.28$ .



**Fig. 4.** Same as Fig. 1 but for SFDM restricted to  $|\epsilon| < 0.4$ .

for larger  $M/L_*$  in Appendix B.2. To confirm this, we did the fits again but required that the galaxies are in the MOND-limit,  $|\epsilon| < 0.4$ . For the rationale behind the precise value 0.4, please refer to Appendix D.2.3.

As one can see from Fig. 2, the fits with the requirement  $|\epsilon| < 0.4$  are not much worse than those without. The averaged  $Q_*$  is now smaller than in MOND; for the  $Q = 1$  galaxies, the median stellar disk  $M/L_*$  is about 10% smaller than for MOND. This confirms superfluids outside the MOND limit as one reason for the large  $Q_*$  values in SFDM, see also Appendix D.2.2.

Another reason why SFDM does not universally give smaller  $Q_*$  than MOND is that the best-fit  $Q_*$  depends on the type of galaxy. In SFDM,  $Q_*$  is systematically smaller for galaxies with relatively large accelerations  $a_b$ , but not for those with small accelerations. This can be seen for example in Fig. 5 which shows the best-fit  $Q_*$  of each galaxy in SFDM relative to the best-fit  $Q_*$  for MOND as a function of the observed asymptotic rotation velocity  $V_{\text{flat}}$ . A larger  $V_{\text{flat}}$  is associated with larger accelerations – this is where SFDM systematically gives smaller  $Q_*$  than MOND. There are similar trends for surface brightness and the gas fraction; both also correlate with the accelerations  $a_b$ , see Appendix D.2.4 for more details.

The reason for this trend is that the smaller  $a_0$  value of SFDM makes the acceleration  $\sqrt{a_0 a_b}$  smaller than in MOND. This acceleration  $\sqrt{a_0 a_b}$  is dominant at small  $a_b$ , so that SFDM needs more baryonic mass than MOND to get the same total accelera-

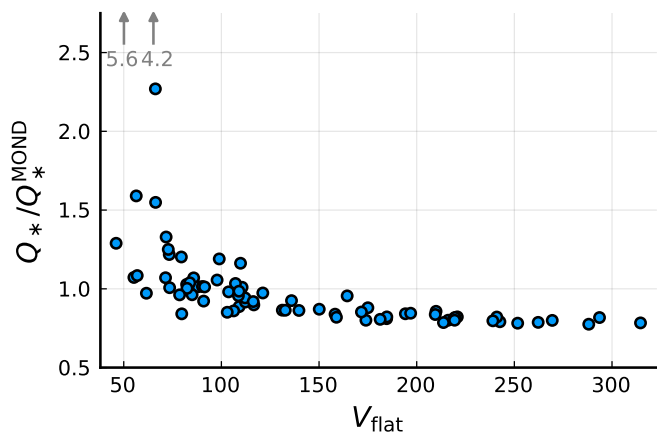


**Fig. 5.** The best-fit  $Q_*$  values in SFDM restricted to the MOND limit ( $|\varepsilon| < 0.4$ ) relative to those for MOND as a function of the observed flat rotation velocity  $V_{\text{flat}}$ . Gray arrows indicate two outliers with relatively large  $Q_*/Q_*^{\text{MOND}}$ . Some galaxies can barely satisfy the condition  $|\varepsilon| < 0.4$  and therefore give a bad fit to the data. Their best-fit  $Q_*$  is meaningless and they are excluded in this plot. Specifically, we exclude galaxies that have both  $\varepsilon > 0.38$  and  $\chi^2 > 100$ . We also show only the  $Q = 1$  galaxies.

tion (at least if  $a_{\text{SF}}$  is negligible). This is explained in more detail in Appendix B.1

Such trends of the stellar  $M/L_*$  with galaxy properties are not expected from stellar population synthesis models (Schombert et al. 2019). This disfavors SFDM, especially compared to MOND which does not show such trends (McGaugh 2004).

## 5.2. Tension with strong lensing

Irrespective of the resulting  $M/L_*$  values, there is a price to pay for enforcing the MOND-limit in SFDM. A MOND-like rotation curve in the MOND-limit  $|\varepsilon_*| \ll 1$  can only be achieved by reducing the acceleration created by the gravitational pull of the superfluid. As a result, the total dark matter mass in those galaxies,  $M_{200}^{\text{DM}}$ , comes out to be quite small. Here,  $M_{200}^{\text{DM}}$  is the dark matter mass within the radius  $r_{200}$  where the mean dark matter density drops below  $\rho_{200} = 200 \times 3H^2/(8\pi G)$  with the Hubble constant  $H$ . We adopt  $H = 67.3 \text{ km}/(\text{s} \cdot \text{Mpc})$ .

A small  $M_{200}^{\text{DM}}$  is not a problem for fitting SFDM to the observed rotation curves, but it is a problem if one *also* wants to fit strong lensing data. Indeed, Hossenfelder & Mistele (2019) previously found that SFDM requires ratios  $M_{200}^{\text{DM}}/M_b \gtrsim 1000$  to fit strong lensing constraints, where  $M_b$  is the total baryonic mass. Requiring a rotation curve in the MOND-limit  $|\varepsilon_*| \ll 1$  for the SPARC galaxies produces average masses at least an order of magnitude smaller.

To illustrate the problem with strong lensing, we have in Fig. 6 plotted the (logarithm of) the total baryonic and the maximum possible total dark matter mass given our requirement  $|\varepsilon| < 0.4$  in comparison to the values found in Hossenfelder & Mistele (2019). For this, we used  $Q_* = 1$  for all SPARC galaxies because the precise stellar mass-to-light ratio is irrelevant here. ‘Maximum possible’ here refers not only to the requirement  $|\varepsilon| < 0.4$  but also to uncertainties in how to determine the radius where the superfluid core is matched to an NFW halo: We use the transition radius that gives the largest total dark matter mass. See Appendix D.3 for details.

The best SFDM fits to strong lensing data tend to have  $M_b \gtrsim 10^{11} M_\odot$  and  $M_{200}^{\text{DM}}/M_b \gtrsim 1000$ . In contrast, despite our

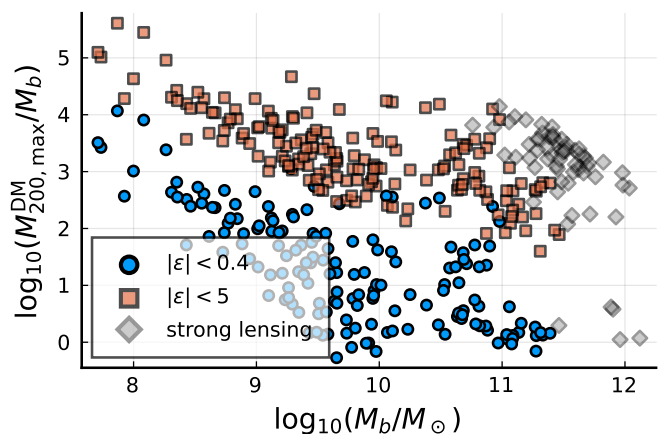


**Fig. 6.** The total baryonic mass  $M_b$  versus the upper bound  $M_{200,\text{max}}^{\text{DM}}/M_b$  of the ratio of the total dark matter mass  $M_{200}^{\text{DM}}$  and  $M_b$  for the SPARC galaxies. This is for  $(M/L_*)_{\text{disk}} = 0.5$  and  $(M/L_*)_{\text{bulge}} = 0.7$ . The upper bound comes from the condition that the rotation curve is in the proper MOND limit ( $|\varepsilon| < 0.4$ , blue circles) or at least the pseudo-MOND limit ( $|\varepsilon| < 5$ , red squares). Also shown are the best-fit results from the strong lensing analysis Hossenfelder & Mistele (2019), where we use their best-fit  $M_{200}^{\text{DM}}$  for the vertical axis.

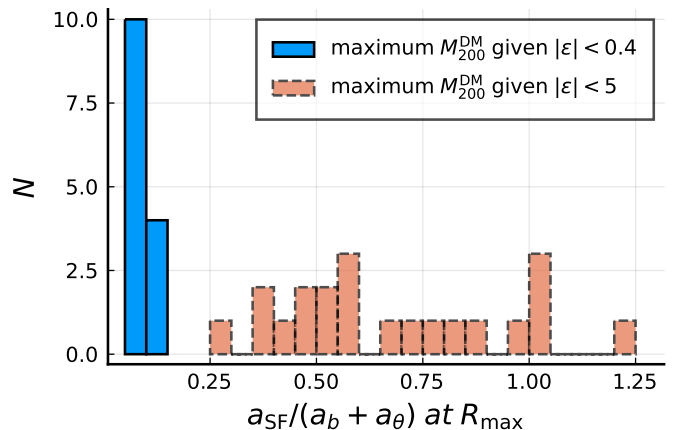


**Fig. 7.** Histogram of  $a_{\text{SF}}$  relative to  $a_b + a_\theta$  at the last rotation curve data point at  $R = R_{\text{max}}$ . This is for the maximum possible total dark matter mass  $M_{200}^{\text{DM}}$  given the condition  $|\varepsilon| < 0.4$  (blue) and  $|\varepsilon| < 5$  (red). We take  $Q_* = 1$  for all galaxies and show only the galaxies with  $M_b > 10^{11} M_\odot$  relevant for strong lensing.

generous NFW matching procedure, the SPARC galaxies with  $M_b > 10^{11} M_\odot$  have  $M_{200}^{\text{DM}}/M_b < 10$  when restricted to have rotation curves in the MOND limit  $|\varepsilon| < 0.4$ . This is a stark contrast.

The SPARC galaxies don’t reach baryonic masses quite as large as the lensing galaxies from Hossenfelder & Mistele (2019). But from Fig. 6 it seems clear that the trend goes into the wrong direction: The larger the galaxy, the smaller the maximum possible  $M_{200}^{\text{DM}}/M_b$  (given  $|\varepsilon| < 0.4$ ).

To study this closer, we did another calculation in which we allow galaxies into the pseudo-MOND-limit. Concretely, we redid the maximum  $M_{200}^{\text{DM}}/M_b$  calculation with the requirement  $|\varepsilon| < 5$ . The precise value 5 is again somewhat arbitrary. We explain why this is a pragmatic choice in Appendix D.2.3. We see from Fig. 6 that in the pseudo-MOND-limit galaxies with  $M_b > 10^{11} M_\odot$  still have smaller total dark matter masses than what is required for strong lensing, although the problem is less severe than in the proper MOND-limit.



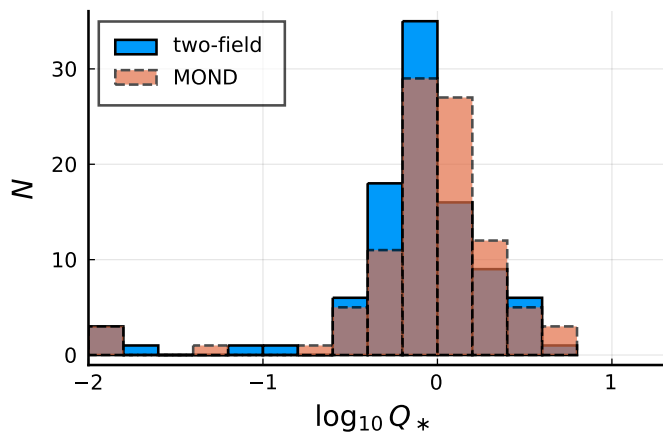


**Fig. 8.** Same as Fig. 1 but for two-field SFDM.

The pseudo-MOND-limit, however, is unsatisfactory for two reasons. First, it relies sensitively on ad-hoc finite-temperature corrections of SFDM that may be unphysical. Second, the pseudo-MOND-limit has the disadvantage that the acceleration from the superfluid,  $a_{\text{SF}}$ , can be significant. If  $a_{\text{SF}}$  is significant, we do not naturally get the MOND-type galactic scaling relations, since then the superfluid boundary condition must be adjusted for each galaxy to get the correct total acceleration. In this case, SFDM loses its advantage over CDM despite the phonon force being close to  $\sqrt{a_0 a_b}$ .

Fig. 7 shows the size of  $a_{\text{SF}}$  relative to  $a_b + a_\theta$  at the last rotation curve data point at  $R = R_{\text{max}}$ , assuming the maximum total dark matter masses from Fig. 6. Indeed, for the pseudo-MOND limit,  $a_{\text{SF}}$  is significant for the galaxies with  $M_b > 10^{11} M_\odot$  relevant for strong lensing. This is despite SFDM having a very cored dark matter profile. Thus, also with the pseudo-MOND limit, we cannot naturally get MOND-like rotation curves and strong lensing at the same time.

### 5.3. Two-field SFDM

For two-field SFDM, the  $Q_*$ -distribution (Fig. 8) and the corresponding CDF (Fig. 2) are similar to those of standard SFDM. However, the two-field model is constructed so that it is easier for the phonon force to be close to the MOND-like value  $\sqrt{a_0 a_b}$ . For this reason, the best fits for two-field SFDM all have  $|\varepsilon_*| \ll 1$ , as expected (Fig. 3). Only for two galaxies (NGC6789, UGC0732) does  $\varepsilon_*$  become larger than 0.1. Its largest value is 0.36 for NGC6789. See Appendix D.4 for more details.

Thus, two-field SFDM can easily have large dark matter masses and  $|\varepsilon_*| \ll 1$  at the same time. It does not have the same problem with strong lensing as the proper MOND limit  $|\varepsilon_*| \ll 1$  of standard SFDM. Two-field SFDM does, however, still have a problem with strong lensing similar to the pseudo-MOND-limit of standard SFDM. Large total dark matter masses imply that the rotation curve receives significant corrections from the superfluid's gravitational pull  $a_{\text{SF}}$ . This is despite two-field SFDM having, like standard SFDM, a very cored density profile. For this reason, large total dark matter masses imply a rotation curve that is not naturally MOND-like.

To illustrate this problem we depict in Fig. 9 the maximum possible total dark matter mass for the two-field model, given the requirement that  $a_{\text{SF}}$  is at most 30% as large as  $a_b + a_\theta$  at the last rotation curve data point at  $R = R_{\text{max}}$ , see Appendix D.5. The scatter in the distribution is smaller in the two-field model

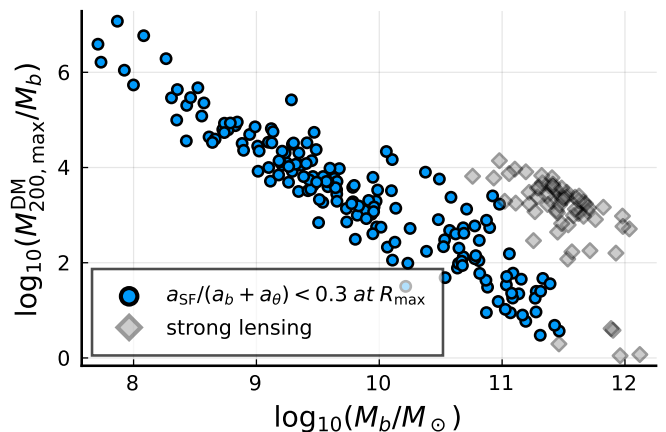


**Fig. 9.** Same as Fig. 6 but for the two-field model and with the requirement that  $a_{\text{SF}}$  is at most 30% as large as  $a_b + a_\theta$  at the last rotation curve data point  $R_{\text{max}}$ .

because it depends less on the details of the baryonic matter distribution, see Appendix D.5. As one can see, in the two-field model the discrepancy with the lensing data is weaker than for the proper MOND-limit  $|\varepsilon_*| \ll 1$  of standard SFDM, but still present. Avoiding this tension with the lensing data would require rotation curves that are even less MOND-like.

## 6. Conclusion

We have found that it is difficult to reproduce the achievements of MOND with the models that have so far been proposed for superfluid dark matter.

*Acknowledgements.* This work was supported by the DFG (German Research Foundation) under grant number HO 2601/8-1.

## References

- Bekenstein, J. & Milgrom, M. 1984, *ApJ*, 286, 7
- Berezhiani, L., Famaey, B., & Khoury, J. 2018, *J. Cosmology Astropart. Phys.*, 1809, 021
- Berezhiani, L. & Khoury, J. 2015, *Phys. Rev. D*, 92, 103510
- Boran, S., Desai, S., Kahya, E. O., & Woodard, R. P. 2018, *Phys. Rev. D*, 97, 041501
- Hossenfelder, S. & Mistele, T. 2019, *J. Cosmology Astropart. Phys.*, 1902, 001
- Hossenfelder, S. & Mistele, T. 2020, *MNRAS*, 498, 3484
- Lelli, F., McGaugh, S. S., & Schombert, J. M. 2016, *AJ*, 152, 157
- Lelli, F., McGaugh, S. S., Schombert, J. M., & Pawłowski, M. S. 2017, *ApJ*, 836, 152
- Li, P., Lelli, F., McGaugh, S., & Schombert, J. 2018, *A&A*, 615, A3
- McGaugh, S. 2019, *ApJ*, 885, 87
- McGaugh, S. S. 2004, *ApJ*, 609, 652
- McGaugh, S. S., Lelli, F., & Schombert, J. M. 2020, *Research Notes of the American Astronomical Society*, 4, 45
- Milgrom, M. 1983a, *ApJ*, 270, 371
- Milgrom, M. 1983b, *ApJ*, 270, 365
- Milgrom, M. 1983c, *ApJ*, 270, 384
- Mistele, T. 2021, *J. Cosmology Astropart. Phys.*, 2021, 025
- Portail, M., Gerhard, O., Wegg, C., & Ness, M. 2017, *MNRAS*, 465, 1621
- Sanders, R. H. 2018, *Int. J. Mod. Phys.*, D27, 14
- Schombert, J., McGaugh, S., & Lelli, F. 2019, *MNRAS*, 483, 1496

## Appendix A: The models

### A.1. Standard SFDM

In standard SFDM, in an equilibrium superfluid core of a galaxy, the phonon field  $\theta$  is determined by the equation (Berezhiani et al. 2018)

$$\nabla \left( \frac{(\nabla\theta)^2 + 2m\left(\frac{2\beta}{3} - 1\right)\hat{\mu}}{\sqrt{(\nabla\theta)^2 + 2m(\beta - 1)\hat{\mu}}} \nabla\theta \right) = \frac{\alpha}{2M_{\text{Pl}}} \rho_b, \quad (\text{A.1})$$

and the field  $\hat{\mu}$  is determined by the Poisson equation

$$\Delta \left( -\frac{\hat{\mu}}{m} \right) = 4\pi G (\rho_b + \rho_{\text{SF}} [\hat{\mu}, \nabla\theta]), \quad (\text{A.2})$$

with the superfluid energy density  $\rho_{\text{SF}}$ ,

$$\rho_{\text{SF}} [\hat{\mu}, \nabla\theta] = \frac{2\sqrt{2}}{3} m^{5/2} \Lambda \frac{3(\beta - 1)\hat{\mu} + (3 - \beta)\frac{(\nabla\theta)^2}{2m}}{\sqrt{(\beta - 1)\hat{\mu} + \frac{(\nabla\theta)^2}{2m}}}. \quad (\text{A.3})$$

Here,  $m$ ,  $\Lambda$ , and  $\alpha$  are model parameters. The quantity  $\hat{\mu}(\mathbf{x}) = \mu_{\text{nr}} - m\phi_N(\mathbf{x})$  is a combination of the (constant) non-relativistic chemical potential  $\mu_{\text{nr}}$  and the Newtonian gravitational potential  $\phi_N(\mathbf{x})$ . It controls how much the superfluid weighs, depending on a boundary condition, see Appendix C.2. The parameter  $\beta$  parametrizes finite-temperature corrections which are needed to avoid an instability (Berezhiani & Khoury 2015). The phonon force  $\mathbf{a}_\theta$  is given by

$$\mathbf{a}_\theta = -\frac{\alpha\Lambda}{M_{\text{Pl}}} \nabla\theta. \quad (\text{A.4})$$

We will mainly use the no-curl approximation for the  $\theta$  equation of motion. That is, for the solution of this equation, which is of the form  $\nabla(g \cdot \nabla\theta) = \mathbf{a}_b$  for some  $g$ , we assume  $g\nabla\theta = \mathbf{a}_b$ . This is a standard approximation in MOND and it works well also for SFDM (Hossenfelder & Mistele 2020).

In the no-curl approximation, the quantity  $\varepsilon_*(\mathbf{x})$  (see Eq. (1)) is useful. As we will see, it controls how closely SFDM resembles MOND. As discussed in Mistele (2021), we have

$$|\mathbf{a}_\theta| = \sqrt{a_0|\mathbf{a}_b|} \cdot \sqrt{x_\beta(\varepsilon_*)}, \quad (\text{A.5})$$

where

$$a_0 = \frac{\alpha^3 \Lambda^2}{M_{\text{Pl}}}. \quad (\text{A.6})$$

and where  $x_\beta(\varepsilon_*)$  is determined by the cubic equation

$$0 = x_\beta^3 + 2\left(\frac{2\beta}{3} - 1\right)\varepsilon_* \cdot x_\beta^2 + \left(\left(\frac{2\beta}{3} - 1\right)^2 (\varepsilon_*)^2 - 1\right)x_\beta - (\beta - 1)\varepsilon_*. \quad (\text{A.7})$$

That is,  $\mathbf{a}_\theta$  is an algebraic function of  $\mathbf{a}_b$  and  $\varepsilon_*$ . This also allows us to write  $\rho_{\text{SF}}$  as a function of  $|\mathbf{a}_b|$  and  $\varepsilon_*$ ,

$$\rho_{\text{SF}}(\varepsilon_*, |\mathbf{a}_b|) = \frac{2}{3} \frac{m^2}{\alpha} \sqrt{a_0|\mathbf{a}_b|} M_{\text{Pl}} \cdot f_\beta(\varepsilon_*), \quad (\text{A.8})$$

where

$$f_\beta(\varepsilon_*) = \frac{x_\beta(\varepsilon_*)(3 - \beta) + 3(\beta - 1)\varepsilon_*}{\sqrt{x_\beta(\varepsilon_*) + (\beta - 1)\varepsilon_*}}. \quad (\text{A.9})$$

For both  $a_\theta$  and  $\rho_{\text{SF}}$ , we have a prefactor proportional to  $\sqrt{a_0 a_b}$  multiplied by a function that depends on  $\varepsilon_*$  and  $\beta$  only. For later use, we record the expansion of this second function for small and large values of  $\varepsilon_*$ . For  $|\varepsilon_*| \ll 1$ , we have

$$\sqrt{x_\beta(\varepsilon_*)} = 1 + \mathcal{O}(\varepsilon_*), \quad (\text{A.10a})$$

$$f_\beta(\varepsilon_*) = (3 - \beta) + \mathcal{O}(\varepsilon_*). \quad (\text{A.10b})$$

For  $\varepsilon_* \gg 1$ ,

$$\sqrt{x_\beta(\varepsilon_*)} = \frac{\sqrt{\beta - 1}}{2\beta - 3} \frac{3}{\sqrt{\varepsilon_*}} + \mathcal{O}(\varepsilon_*^{-3/2}), \quad (\text{A.11a})$$

$$f_\beta(\varepsilon_*) = 3\sqrt{\varepsilon_*} \sqrt{\beta - 1} + \mathcal{O}(\varepsilon_*^{-3/2}). \quad (\text{A.11b})$$

In general,  $f_\beta$  is a monotonically increasing, concave function of  $\varepsilon_*$ , see Fig. A.2. The function  $\sqrt{x_\beta}$  is not monotonic, see Fig. A.1.

To avoid a negative or imaginary  $\rho_{\text{SF}}$  as well as an instability,  $\varepsilon_*$  must be larger than some minimum value  $\varepsilon_{*\text{min}}$ . Berezhiani & Khoury (2015) assume  $\hat{\mu} > 0$ , corresponding to  $\varepsilon_* > 0$ , but this is not required from their Lagrangian. It is an assumption with unclear justification. Here, we are more generous to the model and allow  $\hat{\mu}$  to become negative as long as  $\rho_{\text{SF}}$  stays positive. The corresponding minimum value of  $\varepsilon_*$  is determined by  $\rho_{\text{SF}} = 0$  which is equivalent to  $f_\beta(\varepsilon_{*\text{min}}) = 0$ . For example,

$$\varepsilon_{*\text{min}} = \begin{cases} -\frac{29}{31} \sqrt{\frac{15}{31}} \approx -0.65, & \beta = 1.55 \\ -\frac{1}{4} \sqrt{\frac{3}{2}} \approx -0.31, & \beta = 2 \\ 0, & \beta = 3 \end{cases}. \quad (\text{A.12})$$

With Eq. (1), this translates into a minimum value for  $\hat{\mu}/m$ ,

$$\frac{\hat{\mu}(\mathbf{x})}{m} > \varepsilon_{*\text{min}} \frac{\alpha M_{\text{Pl}} |\mathbf{a}_b(\mathbf{x})|}{2m^2}. \quad (\text{A.13})$$

#### A.1.1. MOND limit

In SFDM, the total acceleration inside the superfluid core of a galaxy can be written as

$$\mathbf{a}_{\text{tot}} = \mathbf{a}_\theta + \mathbf{a}_b + \mathbf{a}_{\text{SF}}, \quad (\text{A.14})$$

where  $\mathbf{a}_\theta$  is the acceleration created by the phonon force,  $\mathbf{a}_{\text{SF}}$  the acceleration stemming from the normal gravitational attraction of the superfluid, and  $\mathbf{a}_b$  that stemming from the mass of the baryons.

For SFDM to make sense, one needs the superfluid to at least approximately reproduce MOND rotation curves in a natural way without, for example, tuning the superfluid mass in each galaxy. Otherwise one does not naturally get the observed MOND-like scaling relations. That is to say, without the MOND-limit of SFDM, one might as well use CDM.

SFDM approximately reproduces MOND rotation curves when the total acceleration  $\mathbf{a}_{\text{tot}}$  approximately has the form  $a_b + \sqrt{a_0 a_b}$ . This corresponds to two conditions. First, the phonon force  $\mathbf{a}_\theta$  must be close to  $\sqrt{a_0 a_b}$ . Second, the superfluid's gravitational pull  $\mathbf{a}_{\text{SF}}$  must be negligible.

The numerical values of the model parameters and the boundary condition of the Poisson equation for  $\hat{\mu}$  determine in which coordinate-range SFDM approximates MOND for a given baryonic mass distribution. Specifically, the MOND-limit corresponds to  $|\varepsilon_*(\mathbf{x})| \ll 1$ . In this  $|\varepsilon_*| \ll 1$  limit, both conditions to reproduce MOND rotation curves are automatically fulfilled:

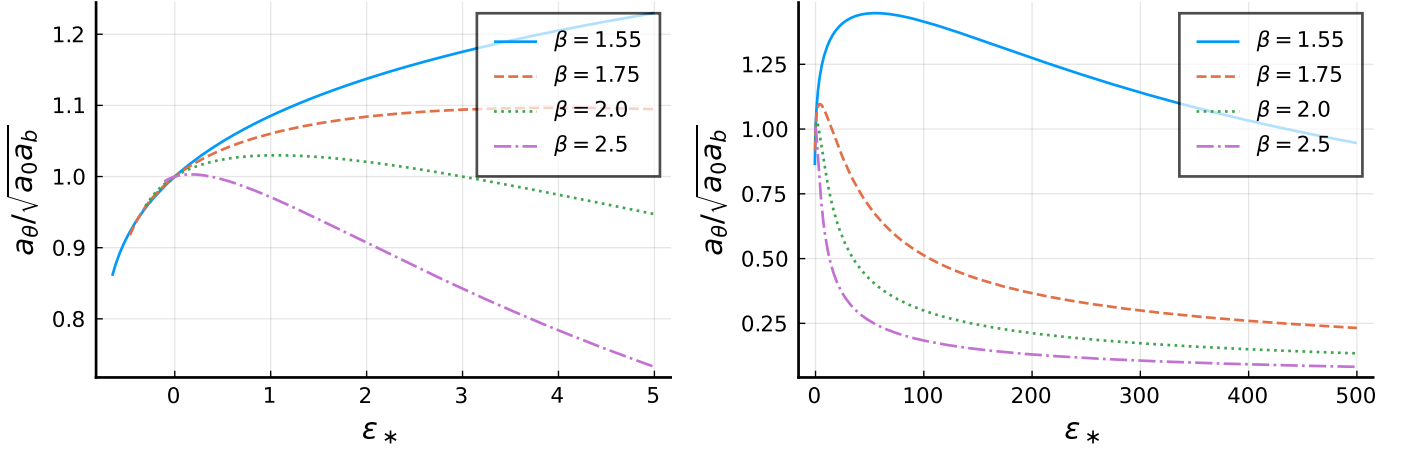


**Fig. A.1.** Left: How close the phonon force  $a_\theta$  is to its MOND limit value  $\sqrt{a_0 a_b}$  as a function of  $\varepsilon_*$  for  $\varepsilon_* < 5$  and for various values of the parameter  $\beta$  that parametrizes finite-temperature corrections. Right: The same up to  $\varepsilon_* = 500$ .

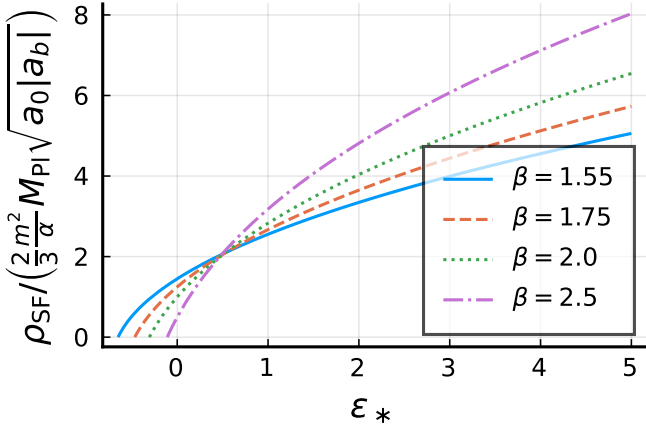


**Fig. A.2.** The function  $f_\beta(\varepsilon_*) = \rho_{\text{SF}} \cdot \left(\frac{2}{3} \frac{m^2}{\alpha} M_{\text{PI}} \sqrt{a_0 |a_b|}\right)^{-1}$  as a function of  $\varepsilon_*$  for different values of  $\beta$ . This is a concave, monotonically increasing function. It does not depend on any model parameters except  $\beta$ .

The phonon force is close to  $\sqrt{a_0 a_b}$  and the superfluid’s gravitational pull  $a_{\text{SF}}$  is negligible. The phonon force is close to  $\sqrt{a_0 a_b}$  because, for  $|\varepsilon_*| \ll 1$ , the (no-curl version of) the phonon field equation Eq. (A.1) has the MOND-like form  $|a_\theta| a_\theta = a_0 a_b$ . This corresponds to the small- $|\varepsilon_*|$  expansion  $\sqrt{x_\beta} = 1$  from Eq. (A.10a). We explicitly show that  $a_{\text{SF}}$  is negligible, i.e. that the second condition is fulfilled, at the end of this subsection.

However, even when  $\varepsilon_*$  is of order 1, deviations of the phonon force from the MOND form  $\sqrt{a_0 a_b}$  remain within the percent range, at least for  $\beta = 2$ , see Fig. A.1. It will therefore in the following be handy to define a “pseudo-MOND limit”,  $\varepsilon_* = \mathcal{O}(1)$ . If this condition is fulfilled, the phonon field no longer satisfies a MOND-like equation, but the acceleration  $a_\theta$  of an isolated<sup>1</sup> galaxy is numerically still relatively close to  $\sqrt{a_0 a_b}$ . One difference to the proper MOND limit  $|\varepsilon_*| \ll 1$  is that now the second condition for having MOND-like rotation curves is not automatically fulfilled. The superfluid’s gravitational pull  $a_{\text{SF}}$  can be significant. So the observed scaling relations are fulfilled naturally only if  $a_{\text{SF}}$  stays sufficiently small, which needs to be checked separately for each solution.

<sup>1</sup> If a galaxy is not isolated, the phonon force may be different than in MOND, since the external field effect will be different since  $\theta$  does not satisfy a MOND-like equation.

A different problem with the pseudo-MOND limit is that it depends sensitively on the details of the ad-hoc finite-temperature corrections introduced in Berezhiani & Khoury (2015) to avoid an instability. For example, the pseudo-MOND limit works only for  $\beta$  close to 2, as can be seen from Fig. A.1, left. Just as these ad-hoc finite-temperature corrections, the pseudo-MOND limit may turn out to be unphysical.

It now remains to show that the superfluid’s gravitational pull  $a_{\text{SF}}$  is negligible in the proper MOND limit  $|\varepsilon_*| \ll 1$ . For simplicity, we assume a point mass baryonic energy density,  $\rho_b(\mathbf{x}) = M_b \delta(\mathbf{x})$ , which gives  $a_b = GM_b/r^2$ . Then, for  $|\varepsilon_*| \ll 1$ , we have  $\rho_{\text{SF}} \propto 1/r$ , see Eq. (A.10b). The superfluid’s mass then is

$$M_{\text{SF}}(r) = M_b \cdot \left(\frac{r}{r_c}\right)^2. \quad (\text{A.15})$$

where

$$r_c^{-2} = \sqrt{2\pi} \frac{m^2}{\alpha} \sqrt{\frac{a_0}{M_b}} \left(1 - \frac{\beta}{3}\right). \quad (\text{A.16})$$

We can now estimate the superfluid’s gravitational pull  $a_{\text{SF}}$  compared to  $a_b + a_\theta$ . Roughly,

$$\frac{a_{\text{SF}}}{a_b + a_\theta} \simeq \frac{(r/r_c)^2}{1 + r/r_{\text{MOND}}}, \quad (\text{A.17})$$

with  $r_{\text{MOND}} = \sqrt{GM_b/a_0}$ . This ratio  $a_{\text{SF}}/(a_b + a_\theta)$  can be larger than a fraction  $\delta$  only at a radius  $r_\delta$  that satisfies

$$r_\delta \gtrsim \delta \frac{r_c^2}{r_{\text{MOND}}} = \delta \cdot \frac{1}{\sqrt{2\pi G}} \frac{\alpha}{m^2} \frac{1}{1 - \frac{\beta}{3}} = 53 \text{ kpc} \cdot \left(\frac{\delta}{10\%}\right), \quad (\text{A.18})$$

where we used the fiducial numerical parameters from Berezhiani et al. (2018) for the last equality. That is, assuming the proper MOND limit  $|\varepsilon_*| \ll 1$ , the superfluid’s mass becomes important only at radii larger than where rotation curves are measured.

#### A.1.2. Reaching the proper MOND limit

As already mentioned in Mistele (2021), reaching the proper MOND limit  $|\varepsilon_*| \ll 1$  is not always possible. To avoid a negative  $\rho_{\text{SF}}$  there is a minimum value for  $\hat{\mu}$ , see Eq. (A.13). Typically,  $\hat{\mu}$  is a decreasing function of galactocentric radius and

the Poisson equation Eq. (A.2) tells us that  $\hat{\mu}/m$  has a derivative of about  $-GM/r^2$  where  $M$  includes both the baryonic and superfluid mass. Using the baryonic mass  $M_b$  as a lower bound on  $M$  then gives a lower bound on  $\hat{\mu}/m$ . Roughly,  $\hat{\mu}/m \gtrsim \hat{\mu}_{\min}(r)/m + GM_b/r$ . This translates into a rough lower bound on  $\varepsilon_*$ ,

$$\varepsilon_* \gtrsim \frac{2m^2 r}{\alpha M_{\text{Pl}}} + \varepsilon_{*\min} = 0.10 + 0.41 \cdot \left( \frac{r}{18 \text{ kpc}} - 1 \right), \quad (\text{A.19})$$

where we used  $a_b = GM_b/r^2$  and the fiducial parameter values from [Berezhiani et al. \(2018\)](#).

Thus, small galaxies can easily reach the proper MOND limit  $|\varepsilon_*| \ll 1$  over the whole range where their rotation curve is measured. One just needs to ensure that the superfluid mass is not too large, which is usually possible.

In contrast, larger galaxies sometimes struggle to satisfy the MOND limit condition  $|\varepsilon_*| \ll 1$ , even when the superfluid mass is as small as possible.

### A.1.3. Naive upper bound on MOND limit dark matter mass

In Appendix A.1.1, we saw that being in the proper MOND limit  $|\varepsilon_*| \ll 1$  restricts the superfluid's gravitational pull  $a_{\text{SF}}$  to be relatively small. Similarly, the MOND limit restricts the total dark matter mass to be relatively small, even if we include the non-condensed phase outside the superfluid core.

To see this, consider a galaxy with a superfluid core in the MOND limit  $|\varepsilon_*| \ll 1$  and, for simplicity, assume a point mass baryonic mass distribution  $\rho_b = M_b \delta(\mathbf{x})$ . Then, the superfluid's mass is  $M_{\text{SF}} = M_b \cdot (r/r_c)^2$ , see Eq. (A.15). In SFDM one usually assumes that the superfluid ends at some finite radius  $r_{\text{NFW}}$  where the superfluid's density is matched to that of an NFW halo. The total dark matter mass  $M_{200}^{\text{DM}}$  can be calculated from

$$M_{200}^{\text{DM}} = \frac{4\pi}{3} r_{200}^3 \rho_{200} = M_{\text{SF}}(r_{\text{NFW}}) + M_{\text{NFW}}(r_{\text{NFW}}, r_{200}). \quad (\text{A.20})$$

Here,  $M_{\text{NFW}}$  denotes the mass of the NFW halo between the radii  $r_{\text{NFW}}$  and  $r_{200}$ . The NFW halo energy density falls off faster than the superfluid energy density, i.e. faster than  $1/r$ . Thus,  $M_{\text{NFW}}$  grows slower than quadratically in  $r$  and we have the inequality

$$\frac{4\pi}{3} r_{200}^3 \rho_{200} < M_b \left( \frac{r_{200}}{r_c} \right)^2. \quad (\text{A.21})$$

That is,

$$\frac{r_{200}}{r_c} < \frac{M_b}{\frac{4\pi}{3} \rho_{200} r_c^3}, \quad (\text{A.22})$$

which is equivalent to

$$\frac{M_{200}^{\text{DM}}}{M_b} < \left( \frac{M_b}{\frac{4\pi}{3} \rho_{200} r_c^3} \right)^2 = \frac{1}{\sqrt{2\pi}} \frac{9}{4} \frac{1}{\rho_{200}^2} \left( \frac{m^2}{\alpha} \right)^3 a_0^{3/2} \sqrt{M_b} \left( 1 - \frac{\beta}{3} \right)^3. \quad (\text{A.23})$$

Numerically, with the fiducial parameter values from [Berezhiani et al. \(2018\)](#) and  $H = 67.3 \text{ km}/(\text{s} \cdot \text{Mpc})$ , this is

$$\frac{M_{200}^{\text{DM}}}{M_b} < 0.9 \cdot \left( \frac{M_b}{10^{10} M_\odot} \right)^{1/2}. \quad (\text{A.24})$$

This is too little for strong lensing even for very massive galaxies, see Appendix D.3. This upper bound is independent of the matching procedure to the NFW halo.

## A.2. Two-field SFDM

To avoid some problems of standard SFDM, [Mistele \(2021\)](#) proposed a two-field SFDM model. Its galactic scale phenomenology is similar to that of standard SFDM.

Two-field SFDM contains two fields  $\theta_+$  and  $\theta_-$  instead of just one field  $\theta$  like standard SFDM. Still, in equilibrium only two non-trivial equations must be solved. One for  $\theta_+$  which carries the MOND-like force and one for the Newtonian gravitational potential  $\phi_N$ . As in standard SFDM, we write the equations in terms of  $\hat{\mu}/m$  where  $\hat{\mu} = \mu_{\text{nr}} - m\phi_N$ ,  $\mu_{\text{nr}}$  is the non-relativistic chemical potential, and  $m$  is the mass of the superfluid's constituent particles. Also as in standard SFDM, the MOND limit of the phonon force is controlled by a quantity  $\varepsilon_* = (2m^2/\alpha M_{\text{Pl}} a_b)(\hat{\mu}/m)$ . Thus, we use the same notation  $\varepsilon_*$  in both models.

This model has two contributions to the superfluid energy density,  $\rho_{\text{SF}+}$  and  $\rho_{\text{SF}-}$ . As discussed in [Mistele \(2021\)](#), usually  $\rho_{\text{SF}-}$  dominates. For our calculation below, we assume that this is the case and neglect  $\rho_{\text{SF}+}$ . We verify that  $\rho_{\text{SF}+}$  is always at most 5% as large as  $\rho_{\text{SF}-}$  at  $R = R_{\text{mid}}$  for the best-fits.

As in standard SFDM, we can get the phonon force from a no-curl approximation as a function of  $a_b$  and  $\varepsilon_*$ . We use the same notation  $a_\theta$  as in standard SFDM. The quantity  $\hat{\mu}/m$  is determined as in standard SFDM just with a different  $\rho_{\text{SF}}$ . Concretely, we have in the no-curl approximation for an equilibrium superfluid

$$a_\theta = \sqrt{a_0 a_b} \sqrt{\sqrt{1 + \frac{\varepsilon_*^2}{4} + \frac{\varepsilon_*}{2}}}, \quad (\text{A.25})$$

and

$$\rho_{\text{SF}} = \rho_{\text{SF}-} = \frac{2M_{\text{Pl}}^2 \hat{\mu}}{r_0^2 m}, \quad (\text{A.26})$$

where  $r_0$  is a parameter of the model.

We use the numerical parameter values from [Mistele \(2021\)](#). That is,  $r_0 = 50 \text{ kpc}$ ,  $a_0 = 0.87 \cdot 10^{-10} \text{ m/s}^2$ , and, unless stated otherwise  $\bar{a} = 10^{-12} \text{ m/s}^2$ . The quantity  $m^2/\alpha$  that enters  $\varepsilon_*$  is a combination of these, namely  $m^2/\alpha = 10^{-7/2} (\bar{a}/a_0)^{1/4} (M_{\text{Pl}}/r_0)$ .

One difference to standard SFDM is that  $\varepsilon_*$  is almost always small so that the phonon force  $a_\theta$  almost always has the MOND-like form  $\sqrt{a_0 a_b}$ . But, in contrast to standard SFDM, a small  $|\varepsilon_*|$  implies only that  $a_\theta \approx \sqrt{a_0 a_b}$ , not that  $a_{\text{SF}}$  is small. Thus, even for  $|\varepsilon_*| \ll 1$  one must check that  $a_{\text{SF}}$  is small in order to have naturally MOND-like rotation curves.

The energy density  $\rho_{\text{SF}}$  reaches zero for  $\hat{\mu} = 0$  in two-field SFDM, i.e.  $\varepsilon_{*\min} = 0$ .

## Appendix B: Comparison to MOND

### B.1. Assuming the MOND limit of SFDM

For SFDM in the MOND-limit we approximately have  $a_{\text{tot}} \approx \sqrt{a_0 a_b} + a_b$ , which, in MOND, would correspond to the interpolation function

$$v_\theta(y) = 1 + \frac{1}{\sqrt{y}}, \quad (\text{B.1})$$

with  $y = a_b/a_0$ .

At baryonic accelerations not much smaller or much larger than  $a_0$ , i.e.  $y = \mathcal{O}(1)$ , the additional acceleration from SFDM is



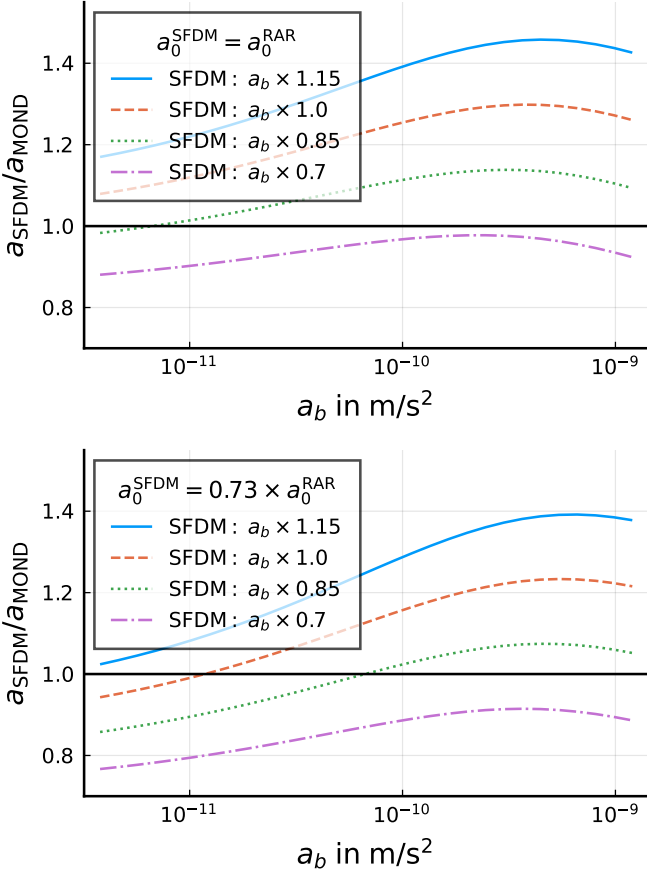


**Fig. B.1.** Top: The ratio of the accelerations  $a_{\text{SFDM}} = a_b v_\theta(a_b/a_0)$  and  $a_{\text{MOND}} = a_b v_e(a_b/a_0)$  as a function of  $a_b$ . Both  $a_{\text{SFDM}}$  and  $a_{\text{MOND}}$  use the same value for  $a_0$ , namely  $a_0 = 1.2 \cdot 10^{-10} \text{ m/s}^2$ , but  $a_{\text{SFDM}}$  uses a baryonic acceleration  $a_b$  that is multiplied by an overall factor relative to  $a_b$  in  $a_{\text{MOND}}$ . Bottom: Same as top, but now  $a_{\text{SFDM}}$  and  $a_{\text{MOND}}$  use different values for  $a_0$ , namely  $a_0^{\text{SFDM}} = 0.87 \cdot 10^{-10} \text{ m/s}^2$  and  $a_0^{\text{RAR}} = 1.2 \cdot 10^{-10} \text{ m/s}^2$ , respectively.

significantly larger than what one obtains from standard MOND interpolation functions such as (Lelli et al. 2017)

$$v_e(y) = \frac{1}{1 - e^{-\sqrt{y}}}. \quad (\text{B.2})$$

It is because of this difference in the interpolation functions that one may naively expect SFDM to require less baryonic mass than standard MOND models, at least in the MOND-limit.

This is illustrated in Fig. B.1, top. The total acceleration in SFDM is always larger than in MOND, if both use the same baryonic  $a_b$ . At intermediate accelerations ( $a_b \sim a_0 \sim 10^{-10} \text{ m/s}^2$ ) the difference between MOND and SFDM is significant. This can be countered by making  $a_b$  in SFDM smaller, i.e. choosing a smaller mass-to-light ratio in SFDM than in MOND.

This discussion so far assumes the same  $a_0$  for both SFDM and MOND. However, in practice, one usually chooses a somewhat smaller value for  $a_0$  in SFDM. Indeed, Berezhiani et al. (2018) chose  $a_0^{\text{SFDM}} \approx 0.87 \cdot 10^{-10} \text{ m/s}^2$ , while MOND typically requires  $a_0^{\text{RAR}} \approx 1.2 \cdot 10^{-10} \text{ m/s}^2$  (Lelli et al. 2017). The motivation of Berezhiani et al. (2018) to choose a lower value is to take into account a possible effect of the superfluid's gravitational pull  $a_{\text{SF}}$ . Indeed, at small accelerations  $a_b$ , the total acceleration in MOND is close to

$$\sqrt{a_0^{\text{RAR}} a_b}, \quad (\text{B.3})$$

while in SFDM we have

$$\sqrt{a_0^{\text{SFDM}} a_b + a_{\text{SF}}}. \quad (\text{B.4})$$

The smaller value of  $a_0$  in SFDM allows to get the same total acceleration even with a non-zero  $a_{\text{SF}}$ . Numerically, the smaller  $a_0$  value is compensated when  $a_{\text{SF}}$  is about  $0.15 \sqrt{a_0^{\text{RAR}} a_b}$ .

Neglecting  $a_{\text{SF}}$ , this smaller value of  $a_0$  makes the total acceleration smaller, so it counters the need for less baryonic mass in SFDM. This is illustrated in Fig. B.1, bottom. The smaller  $a_0$  value has the biggest impact at small accelerations  $a_b$ . At small accelerations,  $a_b \ll a_0$ , SFDM may even require more baryonic mass than MOND, at least if we neglect  $a_{\text{SF}}$ . Indeed,  $a_{\text{SF}}$  is usually negligible in the proper MOND limit  $|\varepsilon_*| \ll 1$ , as discussed above. Thus, assuming the proper MOND limit, we expect to find systematically smaller  $M/L_*$  in SFDM than in MOND for galaxies with large  $a_b$  but not for galaxies with small  $a_b$ . This is roughly what we find in our fits below, see Appendix D.2.4.

## B.2. Caveat: MOND limit

The above discussion applies in the MOND limit of SFDM. Outside this MOND limit, the phonon force does not necessarily have the form  $a_\theta = \sqrt{a_0 a_b}$  and the superfluid's gravitational pull may not be negligible. For example, at  $\varepsilon_* \rightarrow \infty$ , we find that  $a_\theta \propto 1/\sqrt{\varepsilon_*}$ , see Fig. A.1, right. That is, having a large  $\varepsilon_*$  makes  $a_\theta$  small. A smaller acceleration may allow for larger baryonic masses. Thus, having galaxies end up at  $\varepsilon_* \gg 1$  is a way to allow for relatively large mass-to-light ratios in our fits.

One might be skeptical of this argument for the following reason. The argument relies on the total acceleration  $a_{\text{tot}}$  becoming smaller for  $\varepsilon_* \gg 1$ . But this is not necessarily the case. A large  $\varepsilon_*$  does make  $a_\theta$  smaller. But it is possible that the decrease in  $a_\theta$  is compensated by an increase in  $a_{\text{SF}}$ . Indeed, at large  $\varepsilon_*$ , the superfluid's energy density scales as

$$\rho_{\text{SF}} \propto \sqrt{\mu} \propto \sqrt{\varepsilon_* a_b}. \quad (\text{B.5})$$

Thus, at fixed  $a_b$ , a larger  $\varepsilon_*$  makes the superfluid heavier and thus  $a_{\text{SF}}$  larger. For  $\varepsilon_* \rightarrow \infty$ , the acceleration  $a_{\text{SF}}$  can become arbitrarily large. Thus, the total acceleration does not become smaller for  $\varepsilon_* \rightarrow \infty$ , despite the smaller phonon acceleration  $a_\theta$ .

Still, in practice there is a significant window of large values of  $\varepsilon_*$  where the total acceleration does become smaller. To see this explicitly, expand for large large  $\varepsilon_*$ . Then, roughly,  $a_{\text{tot}}$  scales with  $\varepsilon_*$  as

$$a_b + 3 \sqrt{a_0 a_b} \frac{\sqrt{\beta-1}}{2\beta-3} \left( \frac{1}{\sqrt{\varepsilon_*}} + \sqrt{\varepsilon_*} \cdot \frac{2\beta-3}{3-\beta} \cdot \frac{a_{\text{SF}}|_{\varepsilon_*=0}}{\sqrt{a_0 a_b}} \right), \quad (\text{B.6})$$

where we treated  $\varepsilon_*$  as a constant that we can pull out of  $a_{\text{SF}}$ , see Appendix A.1. Thus, at fixed  $a_b$ , the total acceleration  $a_{\text{tot}}$  decreases as a function of large  $\varepsilon_*$  as long as

$$\varepsilon_* < \frac{\sqrt{a_0 a_b}}{a_{\text{SF}}|_{\varepsilon_*=0}} \cdot \frac{3-\beta}{2\beta-3} \approx \frac{r_c^2}{r_{\text{MOND}} \cdot r} \cdot \frac{3-\beta}{2\beta-3} = \frac{6}{2\beta-3} \frac{M_{\text{Pl}}}{r} \frac{\alpha}{m^2}, \quad (\text{B.7})$$

with the MOND radius  $r_{\text{MOND}} = \sqrt{GM_b/a_0}$  and  $r_c$  as defined in Appendix A.1.1. Numerically, for the fiducial parameter values from Berezhiani et al. (2018),

$$\varepsilon_* \lesssim 107 \cdot \left( \frac{5 \text{ kpc}}{r} \right). \quad (\text{B.8})$$

Thus, the total acceleration is a decreasing function of  $\varepsilon_*$  for a significant range of large  $\varepsilon_*$  values so that going to large  $\varepsilon_*$  is one way to allow for relatively large baryonic masses.

## Appendix C: Method

### C.1. Data

As already mentioned in Sec. 3, we use the observed rotation velocity  $V_{\text{obs}}$  directly from SPARC. We do not allow distance or inclination as a fit parameter, so we do not vary  $V_{\text{obs}}$  in our fitting procedure. As also described in Sec. 3, we obtain the baryonic energy density  $\rho_b(R, z)$  from the surface densities provided by SPARC,

$$\rho_b(R, z) = \rho_{\text{gas}}(R, z) + 0.5 \cdot Q_* \cdot \rho_*(R, z) + 0.7 \cdot Q_* \cdot \rho_{\text{bulge}}(\sqrt{R^2 + z^2}). \quad (\text{C.1})$$

The fit parameter  $Q_*$  parametrizes the stellar mass-to-light ratio. For later use, we numerically solve the Poisson equation

$$\Delta\left(-\frac{\hat{\mu}_x}{m}\right) = 4\pi G \rho_x, \quad (\text{C.2})$$

separately for  $\rho_x \in \{\rho_{\text{gas}}, \rho_*, \rho_{\text{bulge}}\}$  using the Mathematica code used in Hossenfelder & Mistele (2020). This allows us to quickly get a solution to the Poisson equation sourced by the full  $\rho_b$  with arbitrary  $Q_*$  by the rescaling

$$\frac{\hat{\mu}_b}{m} = \frac{\hat{\mu}_{\text{gas}}}{m} + 0.5 \cdot Q_* \cdot \frac{\hat{\mu}_*}{m} + 0.7 \cdot Q_* \cdot \frac{\hat{\mu}_{\text{bulge}}}{m}, \quad (\text{C.3})$$

where the quantity  $\hat{\mu}_b/m$  is minus the standard Newtonian gravitational potential up to an additive constant, see also the next subsection. The numerical procedure solves the Poisson equation within a sphere with radius  $r_\infty$  assuming a  $z \rightarrow -z$  symmetry. We assume spherically symmetric boundary conditions for  $\hat{\mu}_b$ . Specifically,

$$\frac{\hat{\mu}_x}{m} \Big|_{\sqrt{R^2+z^2}=r_\infty} = 0. \quad (\text{C.4})$$

This is reasonable for sufficiently large  $r_\infty$ . We use  $r_\infty = 100$  kpc except when the SPARC  $V_{\text{obs}}$  data goes to radii larger than 100 kpc. Then, we increase  $r_\infty$  in steps of 5 kpc until  $r_\infty$  is larger than the maximum radius of the  $V_{\text{obs}}$  data points.

### C.2. SFDM Calculation

We assume that each galaxy's  $V_{\text{obs}}$  data points lie within its superfluid core. This is discussed in more detail in Appendix D.2.7. Then, in SFDM, there are two equations for a galaxy in equilibrium inside the superfluid core. One for the phonon acceleration  $\mathbf{a}_\theta$  and one for the quantity  $\hat{\mu}$  which contains the Newtonian gravitational potential, see Appendix A.1.

Even in a fully-axisymmetric calculation, one can impose spherically symmetric boundary conditions for the fields  $\hat{\mu}$  and  $\theta$  at some large radius  $r_\infty$  (Hossenfelder & Mistele 2020). The value of  $\theta$  at  $r_\infty$  is inconsequential, so one can choose  $\theta(r_\infty) = 0$ . For  $\hat{\mu}$ , its value  $\mu_\infty$  at  $r_\infty$  is important. It determines the size of the superfluid halo and is a free parameter in the boundary conditions. We will use a parameter similar to  $\mu_\infty$  as a free fit parameter in our fitting procedure.

It will be useful to split  $\hat{\mu}$  into a part called  $\hat{\mu}_b$  sourced only by  $\rho_b$  and the rest called  $\hat{\mu}_{\text{SF}}$ . That is,  $\hat{\mu} = \hat{\mu}_b + \hat{\mu}_{\text{SF}}$  with

$$\Delta\left(-\frac{\hat{\mu}_b}{m}\right) = 4\pi G \rho_b, \quad (\text{C.5})$$

$$\Delta\left(-\frac{\hat{\mu}_{\text{SF}}}{m}\right) = 4\pi G \rho_{\text{SF}} [\hat{\mu}_b + \hat{\mu}_{\text{SF}}, \nabla\theta]. \quad (\text{C.6})$$

We use boundary conditions  $\hat{\mu}_b(r_\infty) = 0$  and  $\hat{\mu}_{\text{SF}}(r_\infty) = \mu_\infty$ . We calculate  $\hat{\mu}_b$  as described in the previous subsection.

### C.2.1. A 'simple' approximation

For our fits, we do not do a fully-axisymmetric calculation. Instead, we use an approximation that is much faster to compute. Our approximation mainly consists of using a no-curl approximation for  $\mathbf{a}_\theta$  and assuming spherical symmetry for  $\hat{\mu}_{\text{SF}}$ .

As discussed in Appendix A.1, the no-curl approximation means that we get  $\mathbf{a}_\theta$  as an algebraic function of  $\mathbf{a}_b$  and  $\hat{\mu}$ .

The second part of our approximation is assuming spherical symmetry for  $\hat{\mu}_{\text{SF}}$  in  $\hat{\mu} = \hat{\mu}_b + \hat{\mu}_{\text{SF}}$ . That is, the part of  $\hat{\mu}$  due to the superfluid's self-gravity is spherically symmetric. Only the baryonic part produces an axisymmetric  $\hat{\mu}$ . This is a reasonable approximation for the following reason. A fully-axisymmetric calculation gives a  $\hat{\mu}$  that is non-spherically-symmetric only at relatively small radii. At these radii,  $\hat{\mu}_b$  dominates. At larger radii, even a fully-axisymmetric calculation gives a spherically symmetric  $\hat{\mu}$  (Hossenfelder & Mistele 2020). Indeed, we impose spherically symmetric boundary conditions at larger radii. Only at these larger radii does  $\hat{\mu}_{\text{SF}}$  usually become important.

We calculate  $\hat{\mu}_{\text{SF}}(r)$  from Eq. (C.6) which contains the function  $\hat{\mu}_b(R, z)$ . To solve this equation in spherical symmetry, we need to make a choice of which  $R$  and  $z$  to use in evaluating  $\hat{\mu}_b(R, z)$  for each  $r$ . The same applies to  $a_b(R, z)$ , which enters indirectly through  $\mathbf{a}_\theta$ . We choose  $R = r$  and  $z = 0$ . Different choices may give slightly different results.

For  $\rho_{\text{SF}}$ , we use the expression Eq. (A.8) valid in the no-curl approximation. The function  $f_\beta(\varepsilon_*)$  in this expression for  $\rho_{\text{SF}}$  is known analytically but is relatively slow to evaluate numerically. To speed up the calculation, for a given  $\beta$ , we evaluate  $f_\beta$  as a function of  $\log_{10}(\varepsilon_* - \varepsilon_{*\text{min}})$  on an evenly-spaced grid with grid spacing 0.01 and linearly interpolate between the grid points. We use the resulting linear interpolation in our calculation since it is faster to evaluate numerically than the analytical form of  $f_\beta$ .

Below, we refer to this approximation as the 'simple' approximation. In Appendix C.2.3, we explicitly demonstrate that it works well using a few example galaxies.

### C.2.2. Calculation using the 'simple' approximation

In the 'simple' approximation, we calculate  $\hat{\mu}_b$  as described above in Appendix C.2. From this, we get  $\mathbf{a}_b$  as  $-\nabla\hat{\mu}_b/m$ . For  $\mathbf{a}_\theta$ , we use the no-curl approximation so that we get  $\mathbf{a}_\theta$  as an algebraic function of  $\mathbf{a}_b$  and  $\hat{\mu}_b + \hat{\mu}_{\text{SF}}$ , see Appendix A.1. The remaining part is to calculate  $\hat{\mu}_{\text{SF}}$ . This then also gives  $\mathbf{a}_{\text{SF}}$  as  $-\nabla\hat{\mu}_{\text{SF}}/m$ .

For  $\hat{\mu}_{\text{SF}}$  we assume spherical symmetry and we use the form Eq. (A.8) for  $\rho_{\text{SF}}$  valid in the no-curl approximation. Then, Eq. (C.6) becomes

$$\frac{1}{r^2} \partial_r \left( r^2 \partial_r \left( -\frac{\hat{\mu}_{\text{SF}}(r)}{m} \right) \right) = 4\pi G \rho_{\text{SF}}(\varepsilon_*, |\mathbf{a}_b|), \quad (\text{C.7})$$

where

$$\varepsilon_* = \frac{2m^2}{\alpha M_{\text{Pl}} |\mathbf{a}_b|} \frac{\hat{\mu}_b + \hat{\mu}_{\text{SF}}}{m}. \quad (\text{C.8})$$

The non-spherically symmetric functions  $a_b(R, z)$  and  $\hat{\mu}_b(R, z)$  are evaluated at  $R = r, z = 0$ .

This is a second-order ODE for  $\hat{\mu}_{\text{SF}}$ . As boundary conditions we choose

$$\hat{\mu}'_{\text{SF}}(dr) = 0, \quad (\text{C.9})$$

$$\hat{\mu}_{\text{SF}}(R_{\text{mid}}) + \hat{\mu}_b(R_{\text{mid}}, 0) = \varepsilon \frac{\alpha M_{\text{Pl}} |\mathbf{a}_b(R_{\text{mid}}, 0)|}{2m}. \quad (\text{C.10})$$

With  $dr = 0$ , the first boundary condition is a standard regularity condition at the origin. To avoid numerical issues, we choose a small non-zero value for  $dr$ , usually  $dr = 10^{-8}$  kpc. The second condition corresponds to a choice of  $\varepsilon = \varepsilon_*(R_{\text{mid}})$ , see Eq. (1). It parametrizes how close to the MOND limit  $|\varepsilon_*| \ll 1$  a galaxy is in the middle of the  $V_{\text{obs}}$  data points.

Solutions for  $\hat{\mu}$  are such that they typically reach their minimum allowed value  $\hat{\mu}_{\text{min}}$  (see Eq. (A.13)) at some finite radius. Beyond this radius, assuming a superfluid core makes no sense. Thus, whenever solutions end up with  $\hat{\mu} < \hat{\mu}_{\text{min}}$  at some radius  $dr \leq r \leq R_{\text{max}}$ , we discard them, since we assume all data points to lie within the superfluid core.

Sometimes, Mathematica fails to solve the equations for numerical reasons. This is indicated by its ‘NDSolve’ producing a ‘FindRoot::sszero’, a ‘NDSolveValue::berr’ or a ‘NDSolveValue::evcvmitt’ error that we can check for. In this case, we automatically decrease  $dr$  by factor of 100 and retry.

### C.2.3. Validating the ‘simple’ approximation

Here, we explicitly compare the ‘simple’ approximation described in Appendix C.2.1 against a fully-axisymmetric calculation. For definiteness, we use the best-fit  $Q_*$  and  $f_{\varepsilon_*}$  values for SFDM, see Appendix C.3.

For the fully-axisymmetric calculation we use the Mathematica code from Hossenfelder & Mistele (2020). This code expects boundary conditions in the form  $\hat{\mu}(r_{\infty}) = \mu_{\infty}$  for some  $r_{\infty}$  and  $\mu_{\infty}$ . We choose  $r_{\infty} = 100$  kpc unless stated otherwise. Our ‘simple’ approximation instead uses a value of  $\hat{\mu}_{\text{SF}}(R_{\text{mid}})$  as a boundary condition. To compare our ‘simple’ calculation and the fully-axisymmetric calculation for the same physical boundary conditions, we first do the ‘simple’ calculation with the best-fit values for  $Q_*$  and  $f_{\varepsilon_*}$ . We then evaluate the solution  $\hat{\mu}$  from this ‘simple’ calculation at  $r = r_{\infty}$  and use the resulting value as the boundary condition  $\mu_{\infty}$  for the fully-axisymmetric calculation.

Our ‘simple’ calculation makes two main approximations. First, we use the no-curl approximation for the phonon force. Second, we assume spherical symmetry for  $\hat{\mu}_{\text{SF}}$ . When our simple calculation disagrees with the fully-axisymmetric calculation we want to know which of these two parts is responsible for the deviation. To this end, we do a third calculation where we use the fully-axisymmetric calculation for  $\hat{\mu}$ , but then use the no-curl approximation when calculating  $a_{\theta}$  for the rotation curve. We refer to this as the ‘full+nocurl’ calculation.

In Fig. C.1, left, we show the rotation curve and  $\hat{\mu}/m$  for NGC2403 for the different types of calculation described above. The calculations differ by a few percent at intermediate radii. The ‘full+nocurl’ rotation curve lies pretty much on top of the ‘simple’ rotation curve, while the ‘full’ rotation curve differs from the two others at intermediate radii. Thus, the no-curl approximation is the source of the this difference between the ‘full’ and the ‘simple’ calculations. For  $\hat{\mu}$ , all calculations agree almost perfectly with each other, see Fig. C.1, right.

This same qualitative result holds for DDO064 shown in Fig. C.2. This is an example of a galaxy that is in the proper MOND limit  $|\varepsilon_*| \ll 1$  almost everywhere at  $R_{\text{min}} \leq R \leq R_{\text{max}}$ . The no-curl approximation does not always lead to visible deviations between the ‘full’ and the ‘simple’ calculations. An example is IC2574 where the ‘full’ and ‘simple’ calculations agree almost perfectly with each other, see Fig. C.3.

Thus, our ‘simple’ approximation works well, with the main error being due to the no-curl approximation.

### C.3. Fitting method

For SFDM, we use the two parameters

$$f_Y \equiv \log_{10}(Q_*), \quad (\text{C.11})$$

for the stellar mass-to-light ratio, see Eq. (C.1), and

$$f_{\varepsilon_*} \equiv \log_{10}(\varepsilon - \varepsilon_{*\text{min}}), \quad (\text{C.12})$$

for the superfluid halo, see Eq. (C.12), as fit parameters. Here,  $\varepsilon_{*\text{min}}$  is the minimum possible value of  $\varepsilon_*$  where  $\rho_{\text{SF}}$  vanishes, see Eq. (A.12). We do not vary the model parameters  $m$ ,  $\alpha$ ,  $\Lambda$ , and  $\beta$ . We use Mathematica’s ‘NMinimize’ with the ‘Nelder-Mead’ method to find the smallest  $\chi^2$  for each galaxy,

$$\chi^2 = \frac{1}{N-f} \sum_R \frac{(V_{\text{obs}}(R) - V_c(R))^2}{\sigma_{V_{\text{obs}}}^2(R)}. \quad (\text{C.13})$$

Here,  $N$  is the number of data points in the galaxy,  $f = 2$  is the number of fit parameters,  $\sigma_{V_{\text{obs}}}$  is the uncertainty on the velocity  $V_{\text{obs}}$  from SPARC,  $V_c(R)$  is the calculated rotation curve in SFDM, and the sum is over the data points at radii  $R$ .

We minimize  $\chi^2$  for  $f_Y$  and  $f_{\varepsilon_*}$  in the range Eq. (7) and Eq. (8). When  $f_{\varepsilon_*}$  is too small, it can happen that  $\hat{\mu}$  does not exist with the desired parameters, as discussed in Appendix C.2.2. In this case, we artificially set  $\chi^2 = 10^{10}$ . Then, ‘NMinimize’ continues searching elsewhere.

The ‘NelderMead’ search method is faster than a simple grid search but can get stuck in local minima. To avoid this, we run ‘NMinimize’ three times with different starting points. Of the three results, we use that with the smallest  $\chi^2$ . The first run is with the ‘RandomSeed’ option set to 0, the second with the ‘RandomSeed’ option set to 1, and the third run is with the starting points (0, 0), (−0.5, 0), and (0, −0.5). The third run is to guarantee that the point  $f_Y = 0$  is visited at least once, since this point corresponds to the  $M/L_*$  expected from stellar population synthesis (SPS) models.

To further reduce the needed computation time we round  $f_Y$  and  $f_{\varepsilon_*}$  to 0.01 before any calculation. For (un-rounded)  $f_Y$  and  $f_{\varepsilon_*}$  that give the same rounded values as a previous calculation, we reuse the previous results without a new computation.

This fitting method is much simpler than the MCMC method used in Li et al. (2018). Still, as we will see below in Appendix D.1, we find similar results for the stellar  $M/L$  as Li et al. (2018) for a standard MOND model. In addition, for SFDM we anyway couldn’t set up informative priors on  $f_{\varepsilon_*}$  since there is so far no cosmology from which to infer such a prior.

In the SPARC data, the Newtonian acceleration due to gas sometimes points outwards from the galactic center, not towards it. Usually, such a negative gas contribution is countered by the positive contributions from the stellar disk and bulge such that the total  $a_b$  points to the galactic center. But sometimes this is not the case, especially for small  $f_Y$ . When this happens, we simply ignore the data points where  $a_b$  is negative when calculating  $\chi^2$ .

As a cross-check and as a comparison for SFDM, we also fit the RAR to the SPARC data, i.e. we fit the SPARC data with MOND assuming no curl term and the exponential interpolation function  $v_e$  (Lelli et al. 2017). We will call this the ‘MOND’ model. In this case, we have only one free fit parameter,  $f_Y$ . Thus, when calculating  $\chi^2$ , we set  $f = 1$ . Also, we use the ‘SimulatedAnnealing’ method of Mathematica’s ‘NMinimize’ function with one run instead of the ‘NelderMead’ method with three runs. We do not round  $f_Y$  to 0.01 for these MOND fits.

Below we consider modifications of both the SFDM model and the MOND model. The SFDM-based models will be fitted

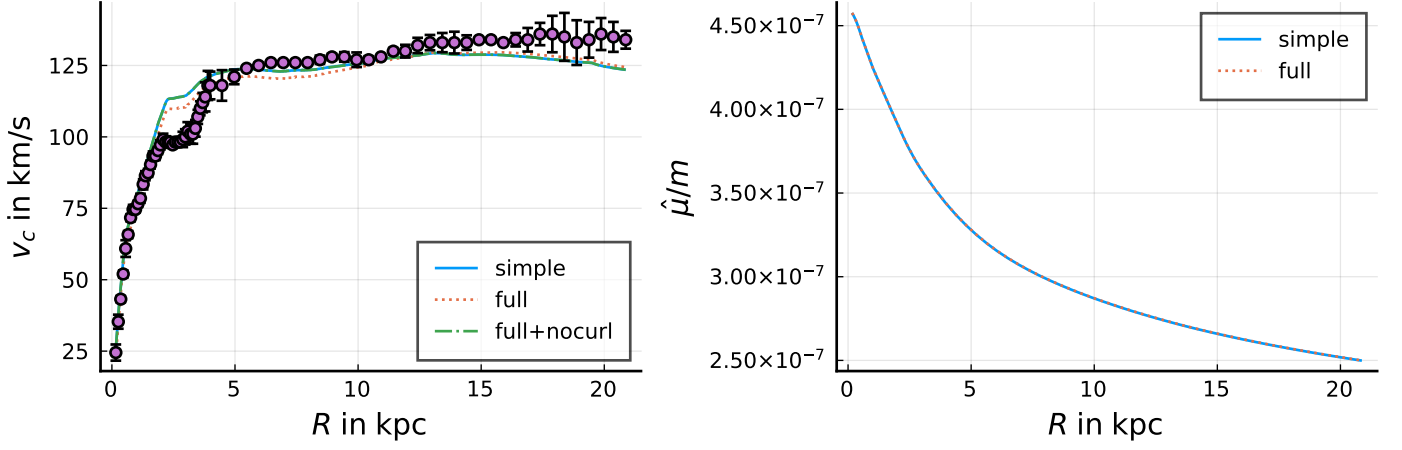


**Fig. C.1.** Left: The rotation curve of NGC2403 for different types of calculations in SFDM (lines) and the observed rotation curve from the SPARC data (circles with error bars). The 'simple' calculation is the approximation described in Appendix C.2.1. The 'full' calculation is the fully-axisymmetric SFDM calculation. The 'full+nocurl' calculation uses the same  $\hat{\mu}(R, z)/m$  as the 'full' calculation but uses a no-curl approximation for the phonon acceleration  $a_\theta$ . This is for the best-fit parameters obtained in Appendix D.2 below. Right: The field  $\hat{\mu}/m$  for the same galaxy and the same models, except for 'full+nocurl' which has the same  $\hat{\mu}/m$  as the 'full' model.

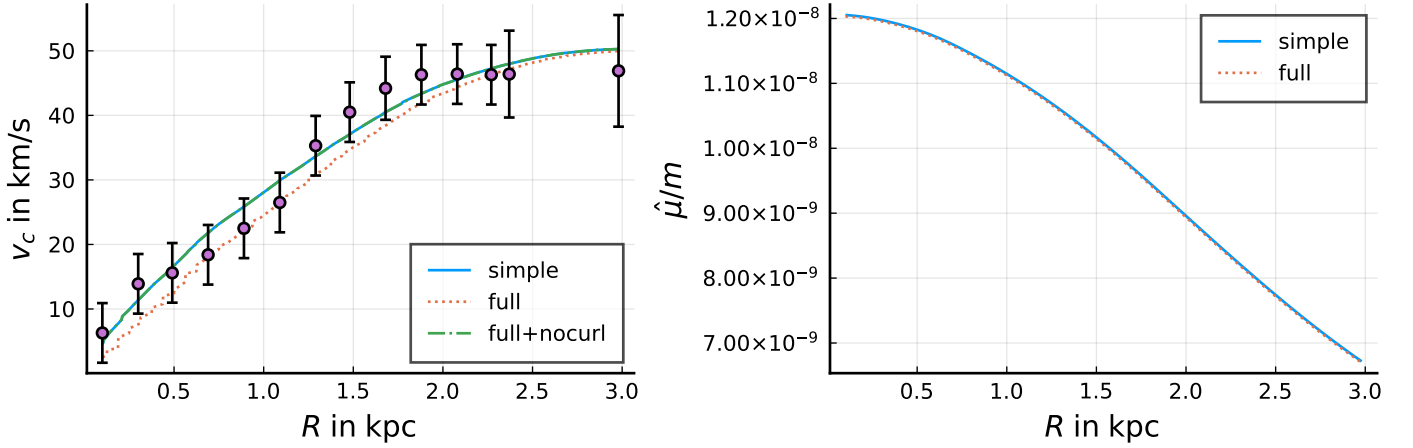


**Fig. C.2.** Same as Fig. C.1 but for DDO064. This is an example of a galaxy in the MOND limit  $|\varepsilon_*| \ll 1$ .

as the 'SFDM' model. The MOND-based models will be fitted as the 'MOND' model. We will discuss the details of these modifications below.

For the SFDM models, we parametrize the total dark matter within the last rotation curve data point  $R_{\max}$  by a parameter  $f_{M_{\text{DM}}}$ ,

$$f_{M_{\text{DM}}} \equiv \log_{10} \left( \frac{M_{\text{DM}}(R_{\max})}{M_{\text{DM}}^{\text{MP}}(R_{\max})} \right), \quad (\text{C.14})$$

where  $M_{\text{DM}}^{\text{MP}}(R)$  is defined by

$$\sqrt{a_0^{\text{SFDM}} a_b(R, z=0)} + a_{\text{SF}}(R, z=0) \equiv \sqrt{a_0^{\text{RAR}} a_b(R, z=0)}, \quad (\text{C.15})$$

with  $a_{\text{SF}} \equiv GM_{\text{DM}}^{\text{MP}}/R^2$  and with the SPS  $M/L_*$  values for  $a_b$ , i.e.  $M/L_* = 0.5$  for the disk and  $M/L_* = 0.7$  for the bulge. The parameter  $f_{M_{\text{DM}}}$  measures how far the dark matter mass at  $R_{\max}$  is away from the reference value  $M_{\text{DM}}^{\text{MP}}$ . This reference value  $M_{\text{DM}}^{\text{MP}}$  is defined such that the associated dark matter acceleration  $a_{\text{SF}}$  counters the difference in  $\sqrt{a_0 a_b}$  between MOND and SFDM due to the different choice for  $a_0$  (see Appendix B.1). Thus,  $f_{M_{\text{DM}}}$  parametrizes how large the dark matter mass is relative to the mass that cancels this  $a_0$  difference.

#### C.4. Two-field SFDM calculation

We can use the same calculation and fitting procedure as for standard SFDM. We simply have to adjust the expression for the superfluid energy density and the algebraic no-curl solution of the phonon force. Apart from that, we adjust the calculation only in two ways that we now explain.

The superfluid energy density  $\rho_{\text{SF}}$  of two-field SFDM is linear in  $\hat{\mu}/m$  and depends on no other fields. This allows to speed up the calculation. For a given galaxy, we first calculate one particular solution  $\hat{\mu}_{\text{SF}}$  of the full, inhomogeneous equation as previously described,

$$\Delta \left( -\frac{\hat{\mu}_{\text{SF}}}{m} \right) = \frac{1}{r_0^2} \frac{\hat{\mu}_b + \hat{\mu}_{\text{SF}}}{m}. \quad (\text{C.16})$$

To get solutions for the same galaxy with different boundary conditions, we can add solutions of the homogeneous equation to the so-obtained  $\hat{\mu}_{\text{SF}}$ . Since we assume spherical symmetry, the solutions to the homogeneous equation are  $A \sin(r/r_0)/r$  for arbitrary  $A$ . To get a solution for some desired boundary condition, we just need to choose an appropriate  $A$ .

For standard SFDM, we used  $\varepsilon_*(R_{\text{mid}})$  in the range  $\varepsilon_{*\text{min}} + 10^{-2}$  to  $\varepsilon_{*\text{min}} + 10^4$  as the boundary condition for  $\hat{\mu}$ . For two-field



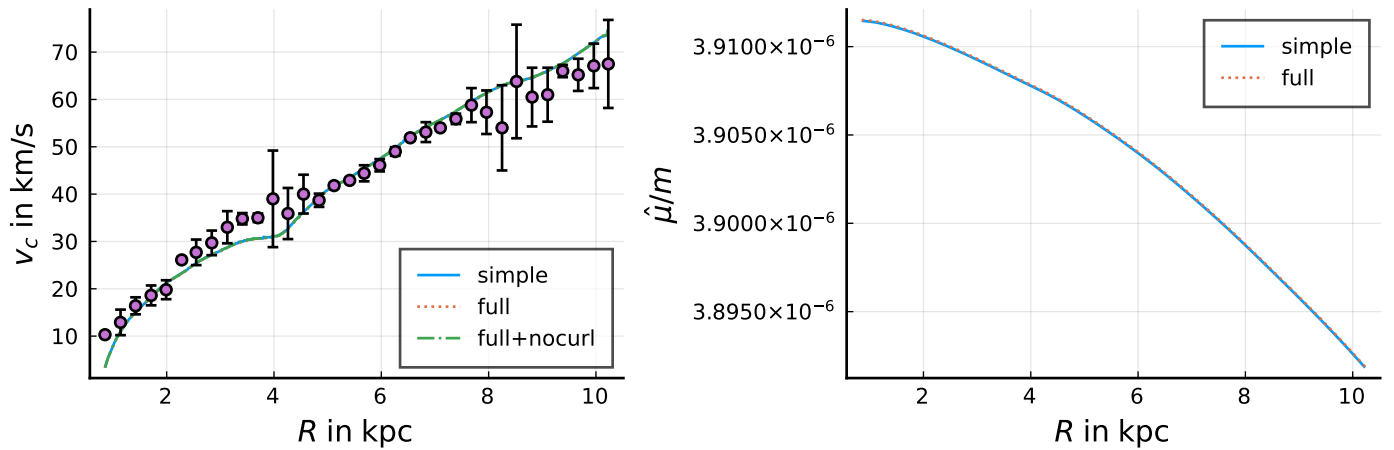


Fig. C.3. Same as Fig. C.1 but for IC2574.

SFDM, we must adjust this range. This is because, in two-field SFDM, the phonon force can more easily reach the MOND limit  $|\varepsilon_*| \ll 1$ , i.e. typical values of  $|\varepsilon_*|$  are much smaller. Thus, we change the range of  $\varepsilon_*(R_{\text{mid}})$  values scanned by our fit code to be

$$10^{-6} \leq \varepsilon_*(R_{\text{mid}}) \leq 1. \quad (\text{C.17})$$

Note that  $\varepsilon_{*\text{min}} = 0$  in two-field SFDM. We will later see that no galaxies end up at the boundaries of this range so it seems to be reasonable.

## Appendix D: Results

### D.1. $M/L_*$ in MOND

Our 'MOND' fit should give results roughly comparable to Li et al. (2018), which also fitted the RAR to SPARC galaxies. A difference is that Li et al. (2018) used a MCMC procedure with Gaussian priors, while we use a simple parameter scan to minimize  $\chi^2$ . We also do not vary distance and inclination and do not separately vary the mass-to-light ratio of the stellar disk and the bulge. As a consequence of this simplified fitting procedure, the distribution of best-fit  $M/L_*$  has more outliers and looks less like a Gaussian in our case compared to Li et al. (2018). This can be seen for example in Fig. D.2, which shows the histograms for the best-fit  $f_Y$  for the galaxies with the SPARC quality flag  $Q = 1$ .

Still, the median best-fit stellar mass-to-light ratios and the best-fit  $\chi^2$  values are similar to those from Li et al. (2018). The median stellar disk  $M/L$  is 0.39. When we restrict ourselves to  $Q = 1$  galaxies, this becomes 0.47. This is shown in Table D.1. This is in reasonable agreement with Li et al. (2018) which obtained 0.50. We show the cumulative  $\chi^2$  distribution in Fig. D.1 which is also in reasonable agreement with Li et al. (2018).

In Fig. D.2, one sees that some galaxies end up at the minimum stellar mass-to-light ratio allowed in our fitting method, corresponding to  $Q_* \approx 0.01$ . If we do not restrict ourselves to  $Q = 1$ , this peak at  $Q_* \approx 0.01$  is even more pronounced. These galaxies with  $Q_* \approx 0.01$  come about as follows. Consider a galaxy where the observed  $V_{\text{obs}}$  is smaller than that computed in MOND. The computed rotation curve can be brought closer to  $V_{\text{obs}}$  by decreasing  $M/L_*$ . It can happen that  $M/L_*$  must be reduced so much that the gas component, which is unaffected by  $M/L_*$ , dominates. When this happens and when  $V_{\text{obs}}$  is still smaller than the computed rotation velocity, the fitting code will continue to decrease  $M/L_*$  to improve  $\chi^2$ . But of course this will only barely change  $\chi^2$  since the gas component dominates, and

the galaxy ends up at the minimum allowed mass-to-light ratio corresponding to  $Q_* = 0.01$ . This does not happen in Li et al. (2018), since varying the distance and inclination can avoid such situations and also because the Gaussian priors discourage going to the minimum allowed  $M/L_*$ .

Thus, the best-fit mass-to-light ratios of the galaxies at  $Q_* = 0.01$  should not be taken seriously. They are an artifact of our simplified fitting procedure. They have a comparably good fit also with larger  $Q_*$ . We have verified that the galaxies at  $Q_* = 0.01$  are gas-dominated at their best-fit  $Q_*$ . To check that our results do not depend on these outlier galaxies, we also include a column in Table D.1 which averages only over the galaxies where the MOND fit gives  $\log_{10} Q_* > -1.5$ . This gives a median stellar disk  $M/L$  of 0.44. This lies between the result for the  $Q = 1$  galaxies and the we got when not restricting the galaxies.

In Table D.1 and Fig. D.1, we also show the results for a fourth quality cut we call 'thermal ok'. This refers to the galaxies where, in our SFDM fit discussed below, a simple estimate shows that all SPARC data points lie within the superfluid core of the galaxy. See Appendix D.2.7 for more details. Here, we just note that this quality cut does not qualitatively change our results.

We show the mean stellar disk mass-to-light ratios in Table D.2. These differ from the median values for all quality cuts because the resulting  $f_Y$  distributions are not Gaussian as already discussed.

### D.2. $M/L_*$ in SFDM

For SFDM, we show the  $\chi^2$  CDF in Fig. D.1 and the  $Q_*$  and  $f_{M_{\text{DM}}}$  histograms for the  $Q = 1$  galaxies in Fig. D.2 and Fig. D.3. The  $\chi^2$  CDF and the  $Q_*$  histogram look qualitatively similar to those from the MOND fit, just with some numerical differences. For example, as for the MOND fit, there are some galaxies at the minimum value  $Q_* = 0.01$ . These are the galaxies that become gas-dominated during the fitting procedure as explained in Appendix D.1. The precise distribution of best-fit  $f_{M_{\text{DM}}}$  values should not be taken too seriously, especially at smaller values. This is because the superfluid halo's Newtonian gravitational pull is often subdominant in SFDM, so that our fitting method cannot really distinguish different  $f_{M_{\text{DM}}}$  values, as long as  $a_{\text{SF}}$  stays subdominant.

Name	all	$Q = 1$	MOND $\log_{10} Q_* > -1.5$	thermal ok
MOND	0.394	0.469	0.443	0.395
MOND $v_\theta$	$\times 0.74$	$\times 0.74$	$\times 0.75$	$\times 0.73$
MOND $v_\theta + a_0^{\text{SFDM}}$	$\times 0.97$	$\times 0.89$	$\times 0.93$	$\times 0.97$
SFDM	$\times 1.18$	$\times 1.04$	$\times 1.10$	$\times 1.25$
SFDM $a_\theta = \sqrt{a_0 a_b}$	$\times 0.92$	$\times 0.87$	$\times 0.88$	$\times 0.92$
SFDM $\beta = 1.55$	$\times 0.90$	$\times 0.87$	$\times 0.90$	$\times 0.91$
SFDM $ \varepsilon  < 5$	$\times 0.96$	$\times 0.89$	$\times 0.92$	$\times 0.96$
SFDM $ \varepsilon  < 0.4$	$\times 0.96$	$\times 0.90$	$\times 0.94$	$\times 0.95$
SFDM $ \varepsilon  < 0.4$ (no bad fits)	$\times 0.94$	$\times 0.89$	$\times 0.92$	$\times 0.94$
two-field	$\times 0.90$	$\times 0.87$	$\times 0.88$	$\times 0.91$
two-field $a_{\min}^{\text{small}}$	$\times 0.90$	$\times 0.87$	$\times 0.88$	$\times 0.91$
two-field $a_b > a_{\min}^{\text{small}}$	$\times 0.90$	$\times 0.87$	$\times 0.88$	$\times 0.91$

**Table D.1.** Median  $0.5 \times Q_*$  for the best-fits for different models and galaxy cuts. Each row corresponds to a different model and each column corresponds to a different cut on the included galaxies. The first row shows the values for the 'MOND' fits, the other rows show the factor relative to the 'MOND' fits.

Name	all	$Q = 1$	MOND $\log_{10} Q_* > -1.5$	thermal ok
MOND	0.534	0.614	0.613	0.558
MOND $v_\theta$	$\times 0.74$	$\times 0.75$	$\times 0.74$	$\times 0.74$
MOND $v_\theta + a_0^{\text{SFDM}}$	$\times 0.96$	$\times 0.96$	$\times 0.96$	$\times 0.96$
SFDM	$\times 1.46$	$\times 1.29$	$\times 1.32$	$\times 1.55$
SFDM $a_\theta = \sqrt{a_0 a_b}$	$\times 0.85$	$\times 0.87$	$\times 0.85$	$\times 0.84$
SFDM $\beta = 1.55$	$\times 0.87$	$\times 0.84$	$\times 0.84$	$\times 0.86$
SFDM $ \varepsilon  < 5$	$\times 0.93$	$\times 0.92$	$\times 0.93$	$\times 0.93$
SFDM $ \varepsilon  < 0.4$	$\times 1.07$	$\times 1.14$	$\times 1.07$	$\times 0.97$
SFDM $ \varepsilon  < 0.4$ (no bad fits)	$\times 0.95$	$\times 0.96$	$\times 0.95$	$\times 0.94$
two-field	$\times 0.84$	$\times 0.88$	$\times 0.84$	$\times 0.82$
two-field $a_{\min}^{\text{small}}$	$\times 0.84$	$\times 0.88$	$\times 0.84$	$\times 0.82$
two-field $a_b > a_{\min}^{\text{small}}$	$\times 0.83$	$\times 0.87$	$\times 0.83$	$\times 0.81$

**Table D.2.** Same as Table D.1 but for the mean instead of the median  $0.5 \times Q_*$ .

### D.2.1. Stellar mass-to-light ratio

Our initial question was whether or not SFDM needs a smaller  $M/L_*$  than standard MOND models. We find that this is not necessarily the case. SFDM has a median stellar disk  $M/L$  of 0.49 for the  $Q = 1$  galaxies. This is not much smaller than MOND. The numerical details depend on whether one considers the mean or the median and on the chosen galaxy cuts, see Table D.1 and Table D.2. Still, a robust finding across all of these choices is that SFDM does not give a significantly smaller  $Q_*$  than MOND.

There are two reasons for this. First, contrary to what one would hope for in SFDM, many galaxies do not end up in the MOND limit  $|\varepsilon_*| \ll 1$ . SFDM does give smaller averaged  $Q_*$  than MOND if the phonon force  $a_\theta$  is close to its MOND-limit value  $\sqrt{a_0 a_b}$ . Second, even in the MOND limit, the best-fit  $Q_*$  values in SFDM are systematically smaller than in MOND only for certain galaxy types. Such trends are not expected from SPS models. It also means we can never say that SFDM universally requires a smaller or larger  $Q_*$  than MOND. We can make such statements only for a given galaxy sample. We will now discuss these two points in more detail.

### D.2.2. Effect of going outside the MOND limit on $M/L_*$

As discussed in Appendix B.2, going to  $\varepsilon_* \gg 1$  allows to make  $a_\theta$  smaller so that a larger  $M/L_*$  is possible. This could be one reason why the averaged  $M/L_*$  is relatively large in SFDM.

As a first check, we show a scatter plot of  $Q_*$  versus  $\varepsilon_*(R_{\text{mid}})$ , see Fig. 3. Indeed, many galaxies have  $\varepsilon_* \gg 1$ . In addition, Fig. 3

shows a correlation between  $\varepsilon_*$  and  $Q_*$ . Galaxies with  $\varepsilon_* \gg 1$  tend to have a larger  $Q_*$ . This fits with the idea that we do not find a smaller  $M/L_*$  for SFDM because many galaxies are not in the MOND limit.

To confirm this, we have re-done the SFDM fit, but with the phonon acceleration  $a_\theta$  replaced by its MOND limit value  $\sqrt{a_0 a_b}$  when calculating rotation curves. The calculation of  $\hat{\mu}$  is left untouched. This is the model shown as 'SFDM  $a_\theta = \sqrt{a_0 a_b}$ ' in, for example, Table D.1 and Fig. D.2. With this model, the trick of going to  $\varepsilon_* \gg 1$  to make the phonon acceleration  $a_\theta$  small does not work. Indeed, the averaged  $M/L_*$  is now significantly smaller than for the original SFDM fit. This result is again robust against different choices for the galaxies we consider and different choices for the averaging function. We can also see explicitly in Fig. D.4 that the distribution of best-fit  $\varepsilon$  values has migrated to smaller values compared to the original SFDM fit.

As a third check, we have re-done the SFDM fit, but with the model parameter  $\beta$  set to 1.55 instead of 2. This choice makes it much harder to make the phonon acceleration  $a_\theta$  small by going to large  $\varepsilon_* \gg 1$ , as can be seen from Fig. A.1. This is the model shown as 'SFDM  $\beta = 1.55$ ' in, for example, Table D.1 and Fig. D.2. If our explanation for the large  $M/L_*$  in SFDM is correct, this modified model should again have significantly smaller  $M/L_*$ . Indeed, this 'SFDM  $\beta = 1.55$ ' model gives results that are comparable to those from the 'SFDM  $a_\theta = \sqrt{a_0 a_b}$ ' model. That is,  $M/L_*$  is now significantly smaller than for the 'SFDM' fit. Similarly, the resulting  $\varepsilon$  values are much smaller than in the original SFDM fit, see Fig. D.4.

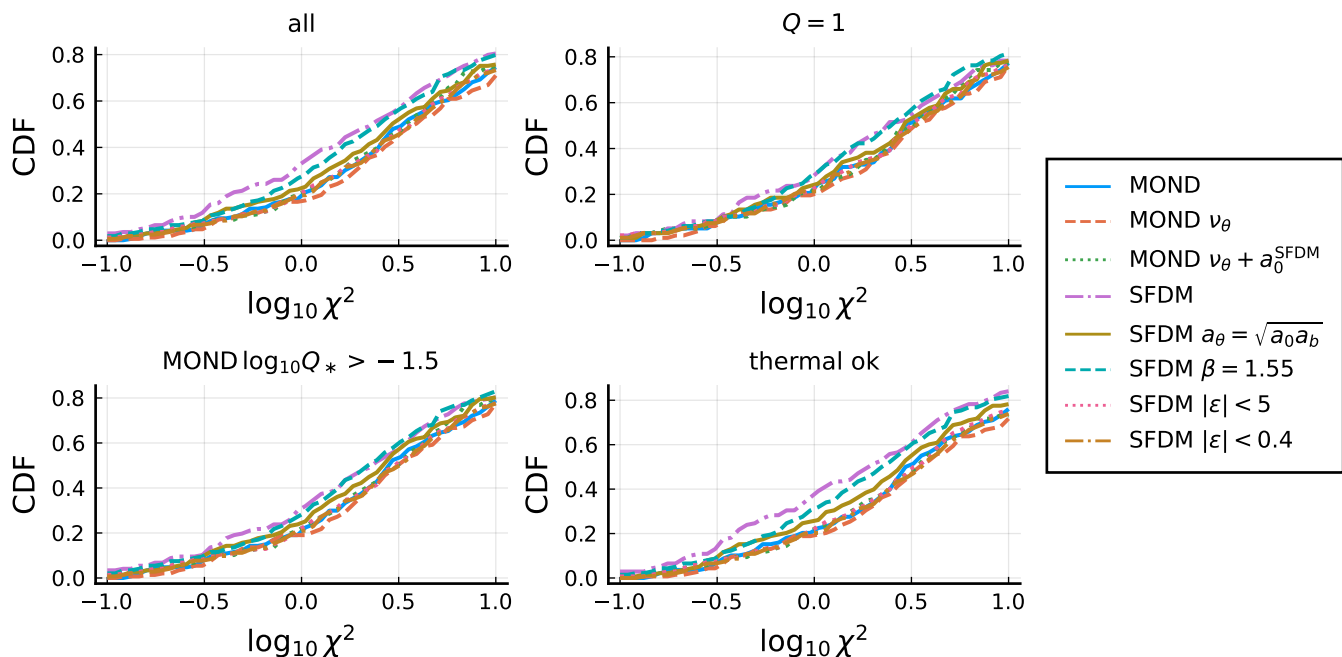


**Fig. D.1.** The  $\chi^2$  CDFs for the different MOND and SFDM models and for different galaxy cuts.

Thus, one reason for the relatively large  $M/L_*$  in SFDM is indeed that many galaxies are not actually in the MOND limit.

### D.2.3. Enforcing the MOND limit

Its MOND limit is one of the main motivations of SFDM, because then rotation curves are naturally MOND-like. This is not the case outside the MOND limit, i.e. when  $\varepsilon_*$  is not small. Thus, our fit results for SFDM go against the original motivation behind SFDM.

We may wonder if large  $\varepsilon_*$  values are really necessary for SFDM to get reasonable fits of the SPARC data. It is possible that our fit code went to  $\varepsilon_* \gg 1$  for little gain in  $\chi^2$ . To check this, we have redone the SFDM fit, but with  $\varepsilon = \varepsilon_*(R_{\text{mid}})$  restricted to  $|\varepsilon| < 0.1$ . Whenever we solve the SFDM equations and find  $|\varepsilon| \geq 0.1$ , we manually set  $\chi^2 = 10^7(1+|\varepsilon|)$  so that the fitting code goes elsewhere. The  $|\varepsilon|$  in  $10^7(1+|\varepsilon|)$  is to help the  $\chi^2$ -minimizing fit algorithm to find small  $|\varepsilon|$ . In this fit, all galaxies are restricted to stay in the proper MOND limit  $|\varepsilon| \ll 1$  of SFDM.

This works, but only for galaxies that are not too large. The restriction  $|\varepsilon| < 0.1$  is impossible to satisfy for many larger galaxies. Our fitting procedure does not find any fit for 38 out of the 169 SPARC galaxies, i.e. 38 galaxies end up with  $\chi^2 > 10^7$ . This is not unexpected since our estimate  $\varepsilon_* \geq 0.1 + 0.4 \cdot (r/18 \text{ kpc} - 1)$  from Eq. A.19 rules out  $|\varepsilon| < 0.1$  for many larger galaxies. Indeed, Fig. D.5, top, shows that the galaxies that cannot be fit with  $|\varepsilon| < 0.1$  tend to be those with  $R_{\text{mid}} \gtrsim 15 \text{ kpc}$ .

Since we set  $\chi^2 = 10^7(1+|\varepsilon|)$  when the condition  $|\varepsilon| < 0.1$  is not satisfied, our fitting algorithm actually minimizes  $|\varepsilon|$  until it satisfies  $|\varepsilon| < 0.1$ . Thus, we can get the minimum possible  $|\varepsilon|$  for each galaxy where  $|\varepsilon| < 0.1$  could not be satisfied. The results are shown in Fig. D.5, bottom. We see that many galaxies only barely fail to satisfy the condition  $|\varepsilon| < 0.1$ . Indeed, if we allowed  $|\varepsilon|$  up to 0.4, almost all galaxies could be fit.

Of course, 0.4 is not that small, so it is debatable whether or not a value  $|\varepsilon| = 0.4$  still counts as the proper MOND limit  $|\varepsilon_*| \ll 1$ . Here, we do not dwell on this point and just re-do our

fit with the condition  $|\varepsilon| < 0.1$  replaced by the condition  $|\varepsilon| < 0.4$ . As expected, we now obtain a fit for almost all galaxies. We do not find a fit for only 4 galaxies. Thus, if by ‘proper MOND limit’ we mean  $|\varepsilon| < 0.1$ , SFDM’s proper MOND limit does not work for larger galaxies. But if we allow  $|\varepsilon|$  up to 0.4, it might.

The resulting best-fit  $\chi^2$  CDF is shown in Fig. D.1. In Fig. D.6, we show the changes in  $\chi^2$  between the ‘SFDM  $|\varepsilon| < 0.4$ ’ fit and the unrestricted ‘SFDM’ fit. The resulting  $\chi^2$  values tend to be worse than for the unrestricted SFDM fit, but generally still acceptable. Indeed, they are quite similar to those of the MOND fit, see the CDF in Fig. D.1.

For some galaxies, the condition  $|\varepsilon| < 0.4$  can barely be satisfied. After satisfying this condition they have basically no freedom left to actually fit the observed rotation curve data and they end up with very bad  $\chi^2$ . Specifically, there are 7 galaxies with  $\varepsilon > 0.38$  and  $\chi^2 > 100$ . Since these are hardly useful in assessing the  $M/L_*$  required in SFDM, we separately list the  $M/L_*$  results with these galaxies excluded in Table D.2 and Table D.1. We also exclude them in Fig. D.6.

Somewhat surprisingly, some galaxies even have a better best-fit  $\chi^2$  with the  $|\varepsilon| < 0.4$  restriction than without, see Fig. D.6. Some of these are just very slightly better than the previous best-fit. For two galaxies it improves by more than 15%, specifically by 46% for NGC1090 and by 19% for NGC2683. For all galaxies with an improved  $\chi^2$ , the corresponding best-fit  $M/L_*$  changes by less than 10%. These differences are insignificant for our purposes. They just show that our fitting algorithm is not perfect and does not always find the very best  $\chi^2$ .

If we exclude the galaxies with a bad  $\chi^2$  because they can only barely satisfy  $|\varepsilon| < 0.4$  as described above, the resulting averaged stellar mass-to-light ratios are between 4% and 11% smaller than for the MOND fit. The numerical details depend on the averaging procedure and the cut of galaxies. We discuss the resulting  $M/L_*$  values in more detail in Appendix D.2.4.

An alternative to the proper MOND limit  $|\varepsilon_*| \ll 1$  is the pseudo-MOND limit discussed in Appendix B.2. At  $\varepsilon_* = O(1)$  (for  $\beta = 2$ ), the phonon acceleration  $a_\theta$  is still numerically close

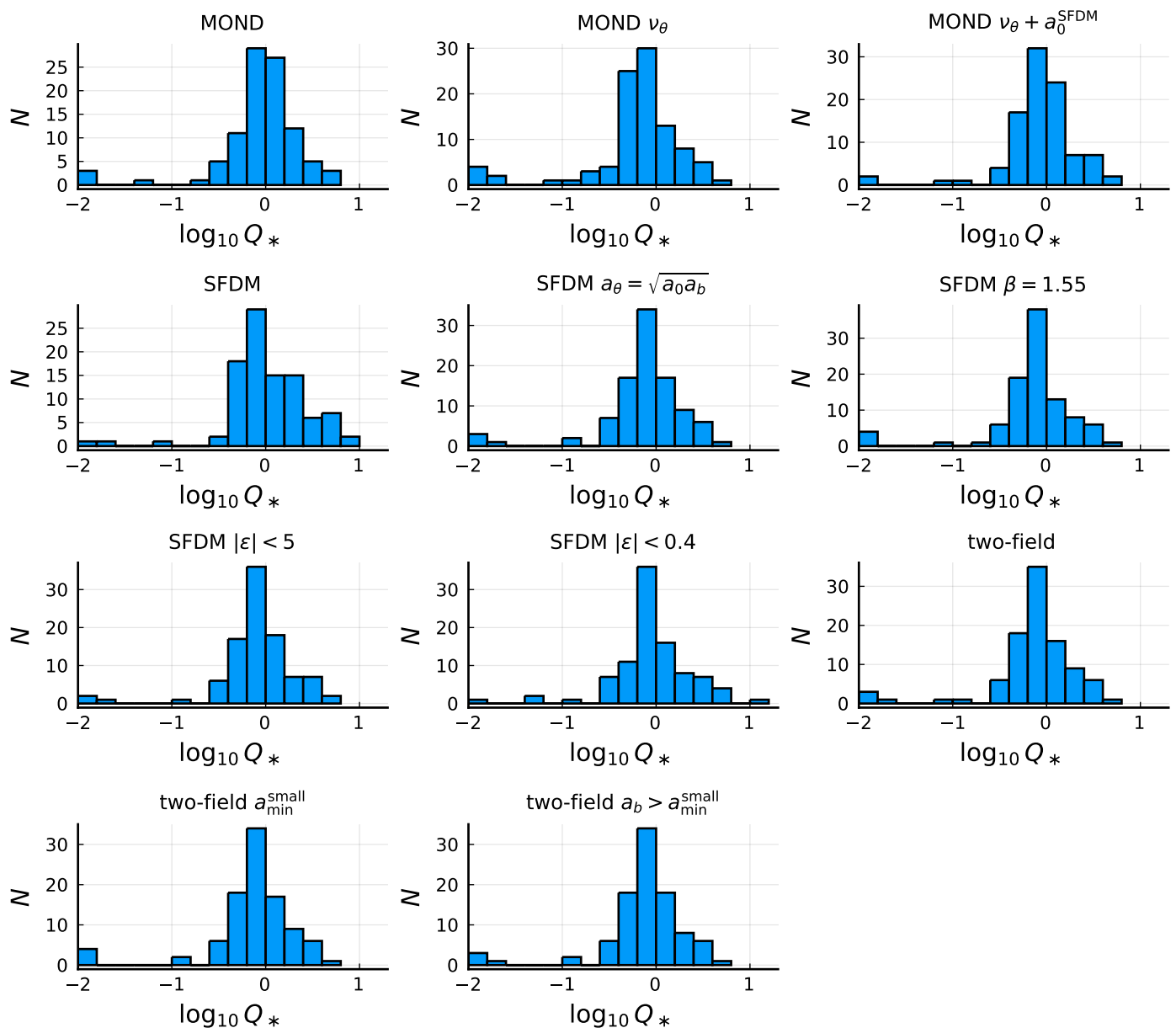


**Fig. D.2.** Histograms of the best-fit  $f_y$  values for the different models restricted to the  $Q = 1$  galaxies.

to its MOND limit value  $\sqrt{a_0 a_b}$  although it does not satisfy a MOND-like equation, see Fig. A.1, left. To test this regime, we have redone the SFDM fit with  $\varepsilon$  restricted to  $|\varepsilon| < 5$ . This is the model shown as ‘SFDM  $|\varepsilon| < 5$ ’ in, for example, Table D.1 and Fig. D.2. Allowing values of  $|\varepsilon|$  up to 5 allows the phonon acceleration  $a_\theta$  to deviate by up to about 5% from its MOND limit value  $\sqrt{a_0 a_b}$  (at  $R = R_{\text{mid}}$ ), see Fig. A.1. The resulting  $\chi^2$  values and stellar mass-to-light ratios are roughly comparable to those of the  $|\varepsilon| < 0.4$  fits. As always, the numerical details depend on the choice of galaxies and on whether we average using the median or the mean.

Thus, fitting the SPARC data does not require  $\varepsilon_* \gg 1$ , i.e. going outside the MOND limit. Both the proper MOND limit and the pseudo-MOND limit also give reasonable  $\chi^2$  values. In this case, the averaged  $M/L_*$  is a bit smaller than in standard MOND models. In Appendix D.2.4, we discuss the  $M/L_*$  of these fits in more detail.

#### D.2.4. Trends of $M/L_*$ with galaxy type

We now come back to the question of why SFDM does not necessarily need a smaller averaged  $M/L_*$  compared to MOND. Above, we already identified one reason, namely that many galaxies are not in the MOND limit  $|\varepsilon_*| \ll 1$ . But this is not the whole story as we will now explain. To this end, we consider the fits with the MOND limit enforced as introduced in the previous subsection. This excludes effects from going outside the MOND limit.

In Appendix B.1, we argued that the MOND limit of SFDM likely requires a systematically smaller  $M/L_*$  than MOND only for high-acceleration galaxies. Galaxies with smaller accelerations may even require a larger  $M/L_*$  than MOND. The main reason is that SFDM has a smaller value of  $a_0$  than MOND, which becomes important at small accelerations. If this is true, having a smaller or larger  $Q_*$  in SFDM is not just a property of the model but also a property of the galaxy sample. An example of this is Fig. 5 which shows the best-fit  $Q_*$  of each galaxy in the



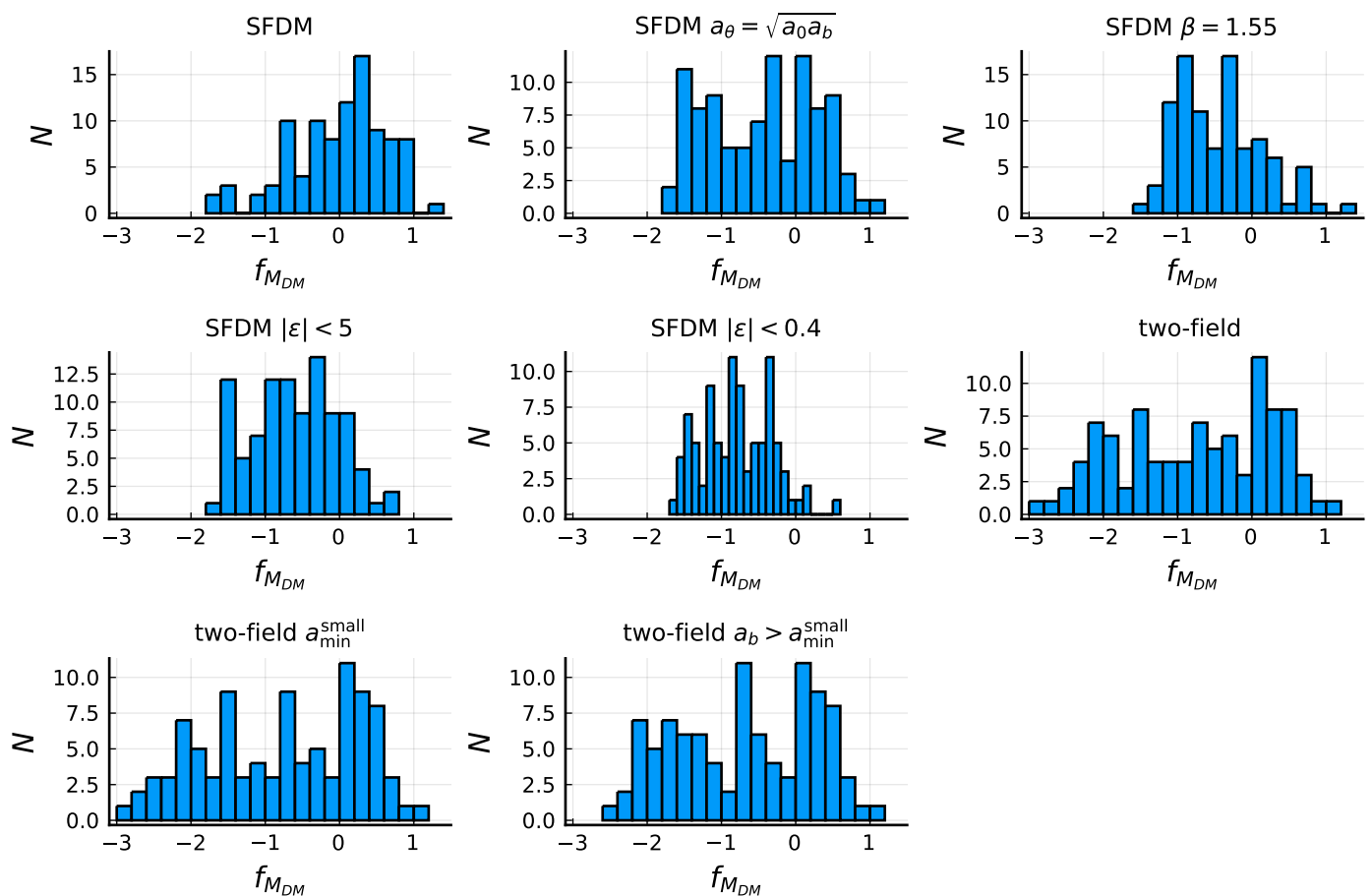


**Fig. D.3.** Histograms of the best-fit  $f_{M_{DM}}$  values for the different models restricted to the  $Q = 1$  galaxies.

‘SFDM  $|\epsilon| < 0.4$ ’ model relative to the best-fit  $Q_*$  for MOND as a function of the observed flat rotation velocity  $V_{\text{flat}}$ . A larger  $V_{\text{flat}}$  is associated with larger accelerations. Indeed, large  $V_{\text{flat}}$  values are where SFDM systematically gives smaller  $Q_*$  than MOND. Similarly, a smaller gas fraction and a larger surface brightness are associated with larger accelerations. The effective surface brightness  $\Sigma_{\text{eff}}$  and the ratio  $M_{H1}/L_{[3.6]}$ , a proxy for gas fraction, of each galaxy are also part of SPARC. And indeed, Fig. D.7 shows that SFDM has a systematically smaller  $M/L_*$  than MOND for galaxies with a large  $\Sigma_{\text{eff}}$  and a small  $M_{H1}/L_{[3.6]}$ .

To further test our understanding, we have redone the MOND fit but using both the interpolation function  $\nu_\theta$  instead of  $\nu_e$  (see Appendix B.1) and the smaller value  $a_0^{\text{SFDM}}$  of  $a_0$ . This should give fits qualitatively similar to those of the MOND limit of SFDM. Indeed, we have verified that the resulting best-fit  $M/L_*$  show similar trends with, e.g.,  $V_{\text{flat}}$  as SFDM. As we explain in Appendix B.1, the different shape of the interpolation function is responsible for the systematically smaller  $M/L_*$  at large accelerations. The smaller  $a_0$  value is responsible for the fact that this is not true at smaller accelerations. Thus, in a MOND model with the SFDM-like interpolation function  $\nu_\theta$  but with the larger  $a_0$  value  $a_0^{\text{MOND}}$ , we would expect to see a smaller  $M/L_*$  consistently across all accelerations. To test this, we have redone the MOND fit with the interpolation function  $\nu_\theta$  but keeping the larger value  $a_0^{\text{MOND}}$  of  $a_0$ . And indeed, this gives a consistently smaller  $M/L_*$  than in MOND. There is no clear trend with, e.g.,  $V_{\text{flat}}$ , see Fig. D.8.

Trends of the stellar  $M/L$  in the [3.6] micron band with galaxy properties are not expected from SPS models (Schombert

et al. 2019). This disfavors SFDM, especially compared to MOND which does not show such trends. If anything, one expects the opposite trend: more massive galaxies should have higher mass-to-light ratios than dwarfs, especially in optical bands.

More precisely, when we do not normalize  $Q_*$  to  $Q_*^{\text{MOND}}$ , our fitting procedure reproduces the SPS expectations neither for MOND nor for SFDM. But this is a consequence of our simplistic fitting procedure. More sophisticated fits do reproduce the SPS expectations for MOND (McGaugh 2004). Moreover, since our simple fitting procedure is suited to identify relative differences between MOND and SFDM, we expect the trends in  $Q_*/Q_*^{\text{MOND}}$  to be robust. It is unlikely that these would be mitigated by a more sophisticated fitting procedure. That is, we expect that this conflict between SFDM and SPS expectations is real.

Fig. 5 and Fig. D.7 show not only that SFDM has a systematically small  $Q_*$  for large accelerations. It also shows that there is more scatter in  $Q_*/Q_*^{\text{MOND}}$  at smaller accelerations. One reason for this scatter is that many of the small-acceleration galaxies are gas-dominated. In gas-dominated galaxies, the formal best-fit value for the stellar mass-to-light ratio, i.e.  $Q_*$ , may not mean much, since  $a_b$  is relatively independent of  $Q_*$ . This allows for more scatter in  $Q_*$ .

#### D.2.5. The Milky Way

Hossenfelder & Mistele (2020) found that SFDM requires about 20% less baryonic mass than standard MOND models to fit the

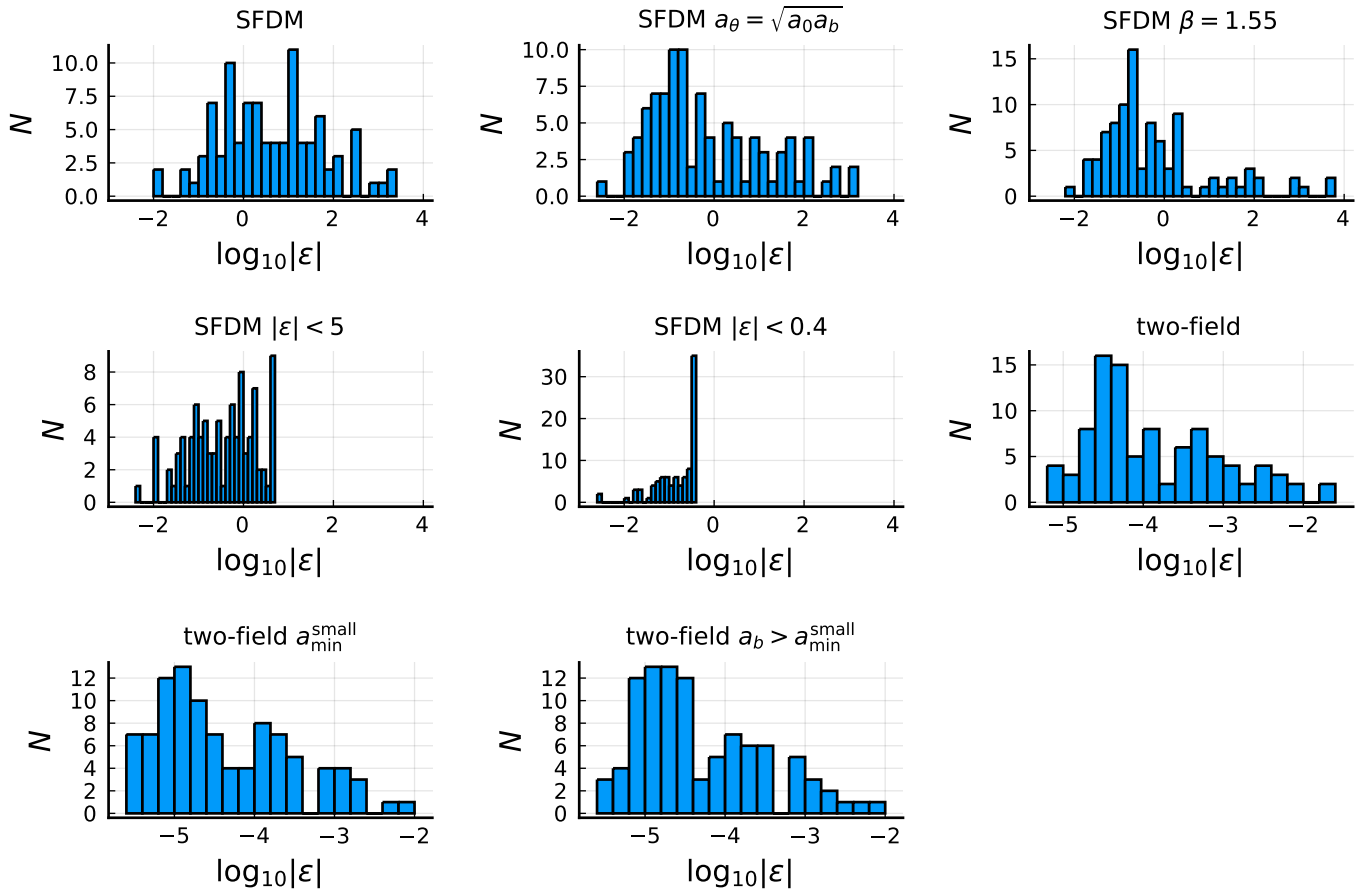


**Fig. D.4.** Histograms of the best-fit values of  $\varepsilon = \varepsilon_*(R_{\text{mid}})$  for the different models restricted to the  $Q = 1$  galaxies.

Milky Way rotation curve at  $R \lesssim 25$  kpc. Specifically, it requires about 20% less baryonic mass than the MOND model from [McGaugh \(2019\)](#). This is a significantly larger difference than what we found, on average, for the SPARC galaxies, see [Table D.1](#) and [Table D.2](#). Here, we confirm and discuss this result.

To confirm the result of [Hossenfelder & Mistele \(2020\)](#), we have fitted the Milky Way with the same method we used for the SPARC galaxies. For this, we used  $\rho_b$  and  $V_{\text{obs}}$  as in [Hossenfelder & Mistele \(2020\)](#). The  $V_{\text{obs}}$  data based on [Portail et al. \(2017\)](#) that is used in [Hossenfelder & Mistele \(2020\)](#) for  $R \lesssim 2$  kpc does not come with error bars. As a simple way to still get a result, we assume an error of 5 km/s for these  $V_{\text{obs}}$  data points. For easier comparison to the SPARC fits, we rescaled the stellar disk and bulge densities such that stellar mass-to-light ratios of 0.5 (for the stellar disk) and 0.7 (for the bulge) correspond to the baryonic mass model used in [McGaugh \(2019\)](#). That is, the factor  $10^{\tilde{f}_y}$  tells us how much less stellar mass SFDM uses compared to the standard MOND model from [McGaugh \(2019\)](#). We find a best-fit  $\chi^2$  of 2.69, a best-fit  $Q_*$  of 0.79, and a best-fit  $\varepsilon$  of 4.37. This confirms the estimate from [Hossenfelder & Mistele \(2020\)](#) of about 20% less baryonic mass compared to standard MOND. This fit stays roughly within the pseudo-MOND limit  $\varepsilon_* = \mathcal{O}(1)$ . With the best-fit parameters,  $\varepsilon_*$  stays below 15 at  $R < 25$  kpc. Thus, the phonon acceleration cannot be much suppressed and cannot allow for an increased  $M/L_*$ , in contrast to galaxies at  $\varepsilon_* \gg 1$ , see [Appendix D.2.2](#).

The Milky Way's  $a_b$  ranges from about  $10^{-9}$  m/s<sup>2</sup> to about  $10^{-10.8}$  m/s<sup>2</sup> at  $R < 25$  kpc for the best-fit parameters. These are

relatively large. So, from the discussion in [Appendix D.2.4](#), a smaller  $M/L_*$  than in MOND is what one would expect.

#### D.2.6. SFDM model parameters

Above, we used the fiducial parameter values from [Berezhiani et al. \(2018\)](#), and kept them fixed during the fitting procedure. Could our conclusions be changed by adjusting these parameters?

Our calculation does not depend on each of the four parameters  $\alpha$ ,  $\Lambda$ ,  $m$ , and  $\beta$  separately. We need only the combinations

$$a_0 = \frac{\alpha^3 \Lambda^2}{M_{\text{Pl}}}, \quad \beta, \quad \frac{m^2}{\alpha}. \quad (\text{D.1})$$

This can be seen directly from the SFDM Lagrangian ([Berezhiani & Khoury 2015](#)) by rescaling the phonon field,  $\theta \rightarrow \theta(\alpha\Lambda/M_{\text{Pl}})^{-1}$ . It also follows from  $(\Lambda m^3)^2 = a_0(m^2/\alpha)^3 M_{\text{Pl}}$ .

First, the acceleration scale  $a_0$ . To reproduce MOND,  $a_0$  must be close to  $10^{-10}$  m/s<sup>2</sup>. Still, we could choose the same value as in standard MOND rather than the somewhat smaller value that [Berezhiani et al. \(2018\)](#) chose. This would give  $M/L_*$  values that are smaller than those for MOND for all galaxies, not just the small-acceleration ones (see [Appendix D.2.4](#)), at least as long as the superfluid's gravitational pull stays negligible. That is, SFDM would give  $M/L_*$  values similar to our 'MOND  $\nu_\theta$ ' fit (see [Appendix D.2.4](#)). These are relatively small. To get closer to  $M/L_*$  values as expected from SPS modeling, one would have to change not only the value of  $a_0$  but also the form of the interpo-

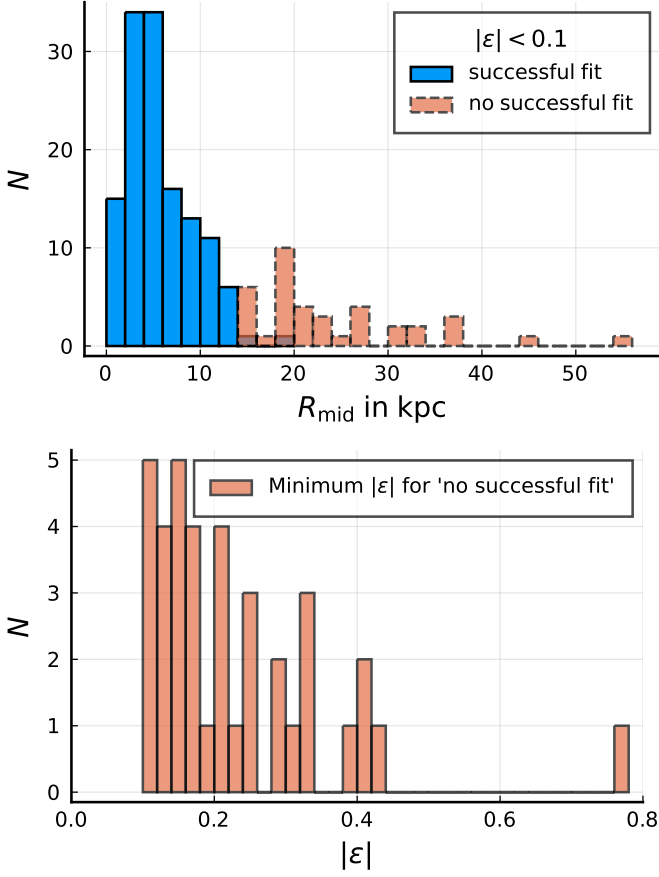


**Fig. D.5.** Top: Histograms of the radius  $R_{\text{mid}}$  for galaxies where we did (blue) and did not (red) find a fit with the restriction  $|\varepsilon| < 0.1$ . We see that only smaller galaxies tend to be able to satisfy the condition  $|\varepsilon| < 0.1$ , consistent with the simple estimate  $\varepsilon_* \gtrsim 0.1 + 0.4 \cdot (r/18 \text{ kpc} - 1)$  from Eq. A.19. Bottom: The minimum possible  $|\varepsilon|$  for the galaxies where we could find no fit with  $|\varepsilon| < 0.1$ . We see that many only barely fail to satisfy  $|\varepsilon| < 0.1$  and we can get a fit for almost all galaxies with  $|\varepsilon| < 0.4$ .

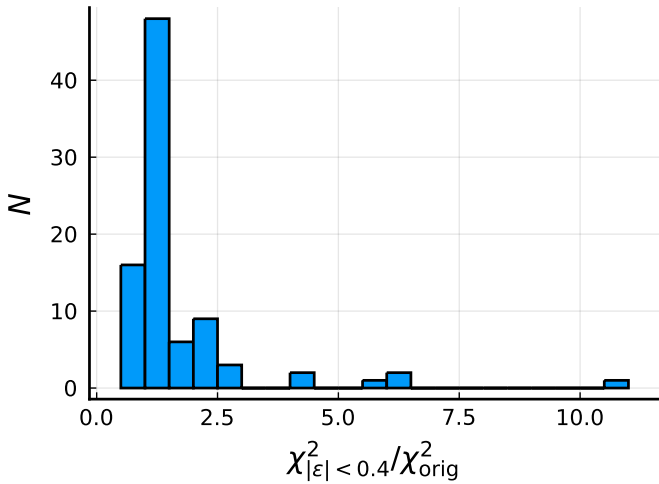


**Fig. D.6.** Histogram of the change in best-fit  $\chi^2$  values for the  $Q = 1$  galaxies when switching from the unrestricted 'SFDM' fit to that with the restriction  $|\varepsilon| < 0.4$ . This is excluding the galaxies that only barely satisfy  $|\varepsilon| < 0.4$  and therefore have a bad  $\chi^2$ , i.e. excluding galaxies with  $\varepsilon > 0.38$  and  $\chi^2 > 100$ .

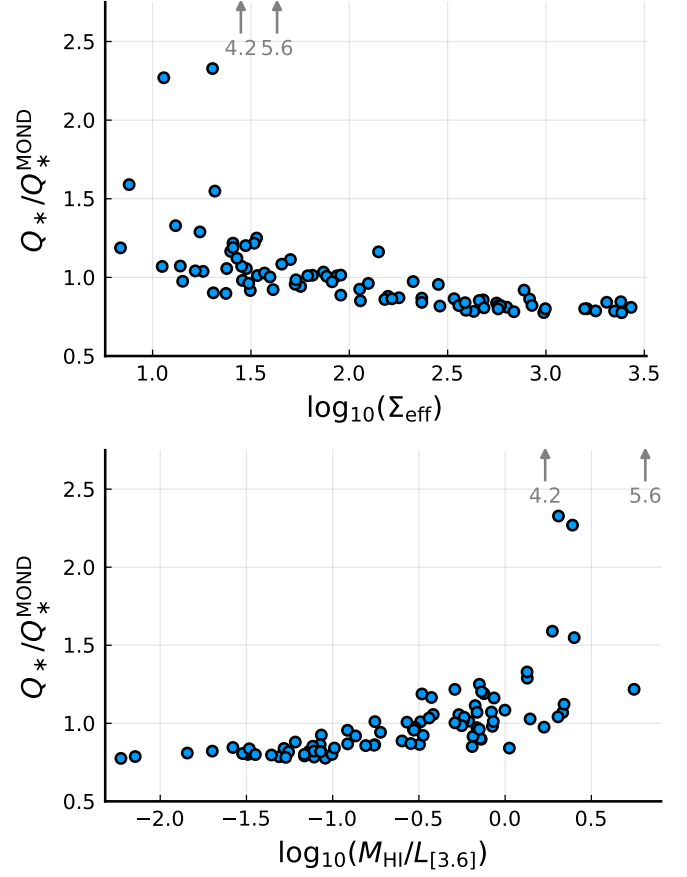


**Fig. D.7.** Top: Same as Fig. 5 but for the effective surface brightness  $\Sigma_{\text{eff}}$  instead of the flat rotation curve velocity  $V_{\text{flat}}$ . Bottom: Same as Fig. 5 but for  $M_{\text{HI}}/L_{[3.6]}$  instead of the flat rotation curve velocity  $V_{\text{flat}}$ .

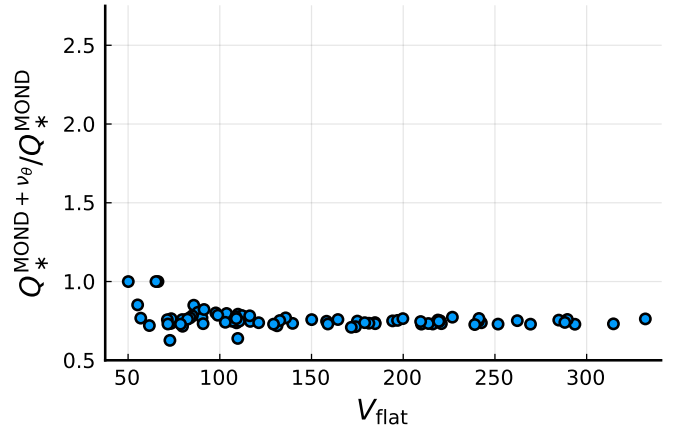


**Fig. D.8.** Same as Fig. 5 but for MOND fits that use the SFDM-like interpolation function  $v_\theta$  instead of  $v_e$  but keep the larger value  $a_0^{\text{MOND}}$  of  $a_0$  (rather than using the smaller value  $a_0^{\text{SFDM}}$ ).

lution function  $v_\theta$ . This might be possible by adjusting the Lagrangian, i.e. changing what is usually called the function  $P(X)$  in superfluid low-energy effective field theories. Exploring this is beyond the scope of this paper.

One effect of the parameter  $\beta$  is that it controls the phonon force outside the proper MOND limit  $|\varepsilon_*| \ll 1$ , see Appendix B.2. For one example ( $\beta = 1.55$ ), we explicitly explored the effect of a different value of  $\beta$  (see Appendix D.2.2). Still, it

is better not to tune this parameter for better fits to the data. This is because the value of  $\beta$  and the form of the finite-temperature corrections it is supposed to represent are completely ad-hoc. So they might turn out to be unphysical. It is better to not rely too sensitively on any specific value of  $\beta$  for the fits.

The combination  $m^2/\alpha$  multiplies both  $\varepsilon_*$  and the superfluid's energy density  $\rho_{\text{SF}}$ . One motivation to change  $m^2/\alpha$  is to make  $|\varepsilon_*|$  small in order to allow more galaxies to reach SFDM's proper MOND limit  $|\varepsilon_*| \ll 1$ , see Appendix A.1.2. The problem with this is that then  $\rho_{\text{SF}} \propto (m^2/\alpha) \cdot f_\beta(\varepsilon_*)$  becomes small as well. Indeed, in this case the problem regarding strong lensing described in Appendix D.3 becomes even worse. Conversely, making  $m^2/\alpha$  larger in order to solve the strong lensing tension means even fewer galaxies can reach the MOND limit  $|\varepsilon_*| \ll 1$ . For example, increasing  $m^2/\alpha$  by a factor of 10 would give  $\varepsilon_* \gtrsim 0.1 + 0.41(r/1.8 \text{ kpc} - 1)$  from Eq. (A.19). Then, only the smallest galaxies could reach the proper MOND limit.

An adjusted function  $P(X)$  might invalidate this argument since this function determines not only the phonon force but also the superfluid's energy density in SFDM. But, again, this is beyond the scope of the present work.

To sum up, adjusting the SFDM model parameters might change some of our conclusions regarding the best-fit  $M/L_*$  values, but probably not in a way that is completely satisfactory from the perspective of SPS models. Moreover, we expect that the tradeoff between having MOND-like rotation curves and producing sufficient strong lensing described in Appendix D.3 remains.

### D.2.7. Thermal radius check

We assume that all SPARC rotation curve data points of a given galaxy lie within this galaxy's superfluid core. This is necessary for one of the main motivations behind SFDM, namely to naturally reproduce MOND-like rotation curves. The superfluid phase ends at the very latest when  $\rho_{\text{SF}}$  reaches zero. Thus, we discard solutions where  $\rho_{\text{SF}}$  vanishes inside the  $V_{\text{obs}}$  data points, as discussed in Appendix C.2.2.

But this may not be sufficient since the superfluid phase may end even before  $\rho_{\text{SF}}$  reaches zero. Consider, for example, the simplest estimate for the radius where the superfluid phase transitions to the non-superfluid phase, the so-called thermal radius  $R_T$  (Berezhiani et al. 2018). According to this estimate, the superfluid phase corresponds to

$$\Gamma > t_{\text{dyn}}^{-1}, \quad (\text{D.2})$$

where  $\Gamma$  is the local self-interaction rate and  $t_{\text{dyn}}$  is the dynamical time. Here,  $\Gamma = (\sigma/m) \mathcal{N} \nu \rho$ , where  $\sigma$  is the self-interaction rate,  $\mathcal{N} = (\rho/m)(2\pi/mv)^3$  is the Bose-degeneracy factor, and  $\nu$  is the average velocity of the particles. Following Berezhiani et al. (2018), we take  $\sigma/m = 0.01 \text{ cm}^2/\text{g}$  and  $t_{\text{dyn}} = R/\nu$ .

As a simple check, we have evaluated the quantity  $\Gamma/t_{\text{dyn}}^{-1}$  for each galaxy at the last  $V_{\text{obs}}$  data point at  $R_{\text{max}}$  for the SFDM best fits. We find that 31 of 169 galaxies violate the condition  $\Gamma > t_{\text{dyn}}^{-1}$  at  $R_{\text{max}}$ . In principle, we should discard these solutions, just as we discard solutions where  $\rho_{\text{SF}}$  reaches zero before  $R_{\text{max}}$ . Here, we do not do this. The reason is that the condition  $\Gamma > t_{\text{dyn}}^{-1}$  is quite ad-hoc. For example, the value of  $\sigma/m$  is chosen ad-hoc and not derived from an underlying Lagrangian. Also, the transition radius derived from  $\Gamma = t_{\text{dyn}}^{-1}$  can, in general, differ wildly from the transition radius derived from the so-called NFW matching procedure (Berezhiani et al. 2018; Hossenfelder & Mistele 2020) where the density and pressure are matched to

those of an NFW halo for a fixed NFW concentration parameter, as discussed in Mistele (2021). This makes any particular choice for discarding solutions based on the thermal or NFW matching somewhat arbitrary.

We avoid this arbitrariness by discarding solutions only based on the criterion that  $\rho_{\text{SF}}$  must be positive. Still, this means we do not discard some solutions that we maybe should discard. This might affect our  $M/L_*$  results. To get a rough idea of possible effects due to this, we also show our results for  $M/L_*$  in Table D.1 and Table D.2 with the 31 galaxies violating  $\Gamma > t_{\text{dyn}}^{-1}$  excluded, labeled as 'thermal ok'. Often, this does not significantly change the  $M/L_*$  fit results, though it does give a larger  $M/L_*$  for example for the 'SFDM' model.

Overall, we expect that actually enforcing the rotation curve data to lie within the superfluid phase does not significantly change our  $M/L_*$  results. But keep in mind that there is a considerable theoretical uncertainty around the transition from the superfluid to the non-superfluid phase. We stress that the tension with strong lensing (see Appendix D.3) is not affected by this uncertainty, because there we anyway choose the transition radius to maximize the resulting total dark matter mass.

### D.3. Tension with strong lensing in SFDM

The proper MOND limit  $|\varepsilon_*| \ll 1$  of SFDM is useful for fitting rotation curves due to its MOND-like phonon force. Above, we saw that most SPARC rotation curves can be reasonably fit with the proper MOND limit  $|\varepsilon_*| \ll 1$ . At least if we count values of  $|\varepsilon_*|$  as large as 0.4 as still satisfying  $|\varepsilon_*| \ll 1$ . But for certain other observables, like strong lensing, the phonon force plays no role. This is because the observation of GW170817 requires that the phonon force does not affect photons (Hossenfelder & Mistele 2019; Sanders 2018; Boran et al. 2018). Thus, the strong lensing signal is produced only by the standard gravitational pull of the mass of the baryons and the superfluid, not by the phonon force.

As a consequence, the MOND limit of SFDM has a serious problem, because the superfluid's energy density is too small to produce significant lensing. Specifically, assuming the whole superfluid core to be in the MOND limit  $|\varepsilon_*| \ll 1$ , a rough upper bound is (see Appendix A.1.3)

$$\frac{M_{200}^{\text{DM}}}{M_b} < \frac{1}{\sqrt{2\pi}} \frac{9}{4} \left(1 - \frac{\beta}{3}\right)^3 \left(\frac{m^2}{\alpha}\right)^3 \frac{\sqrt{a_0^3 M_b}}{\rho_{200}^2} = 0.9 \cdot \left(\frac{M_b}{10^{10} M_\odot}\right)^{1/2}, \quad (\text{D.3})$$

where we assumed the numerical parameter values from Berezhiani et al. (2018). Producing sufficient strong lensing and a superfluid core in the MOND limit seem to be mutually exclusive. Choosing different parameter values may help, especially a larger  $m^2/\alpha$ . But this would imply that fewer galaxies can reach the MOND limit  $|\varepsilon_*| \ll 1$ , as discussed in Appendix D.2.6.

This conclusion can, in principle, be avoided if the superfluid core is in the MOND limit only at smaller radii (where rotation curves are measured), but not at larger radii (where part of the lensing signal comes from). But even in this case there are limits on how large  $M_{200}^{\text{DM}}/M_b$  can be. This is because, given that we have  $|\varepsilon_*| \ll 1$  at relatively small radii, the superfluid's energy density cannot be arbitrarily large at larger radii. Here, we will check whether or not the SPARC galaxies can possibly have a sufficiently large  $M_{200}^{\text{DM}}/M_b$  for strong lensing, if we assume the proper MOND limit for the rotation curves.

Specifically, for each galaxy, we will find the largest possible value  $M_{200,\text{max}}^{\text{DM}}$  of  $M_{200}^{\text{DM}}$  that is compatible with a rotation curve



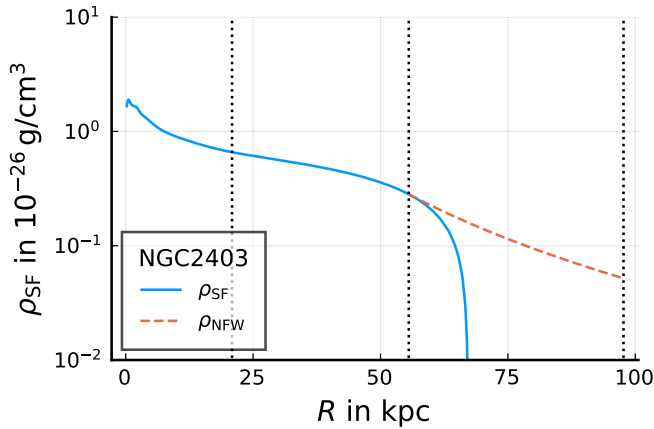


**Fig. D.9.** The dark matter energy density for NGC2403 giving the largest possible  $M_{200}^{\text{DM}}$  compatible with a rotation curve in the MOND limit ( $|\varepsilon| < 0.4$ ). The energy density is that of  $\rho_{\text{SF}}$  (solid blue line) for  $r < r_{\text{NFW}}$  and that of an NFW  $1/r^3$  tail at larger radii (dashed red line). The two contributions are matched to each other at a radius  $r_{\text{NFW}}$  which is chosen to maximize  $M_{200}^{\text{DM}}$ . This is for  $(M/L_*)_{\text{disk}} = 0.5$  and  $(M/L_*)_{\text{bulge}} = 0.7$  and gives  $M_{200}^{\text{DM}} = 9.8 \cdot 10^{10} M_{\odot}$ . The dotted vertical lines denote  $R_{\text{max}}$ ,  $r_{\text{NFW}}$ , and  $r_{200}$ .

in the proper MOND limit. For the requirement that the rotation curve is in the proper MOND limit we impose  $|\varepsilon| < 0.4$  as above.

In SFDM one usually assumes that the superfluid ends at a radius  $r_{\text{NFW}}$  beyond which the energy density is that of an NFW halo (Berezhiani & Khoury 2015; Berezhiani et al. 2018; Hossenfelder & Mistele 2020). For simplicity, we assume the NFW profile  $\rho_{\text{NFW}}(r)$  to be proportional to  $1/r^3$  at the radii of interest, i.e. we continue the superfluid density with an NFW tail instead of a full NFW profile. We do not expect this to significantly affect our results (Hossenfelder & Mistele 2019). The usual procedure for matching the superfluid density to the NFW profile is heuristic and not derived from first principles (Berezhiani et al. 2018; Mistele 2021). To be independent of the details of this matching procedure we match the NFW density  $\rho_{\text{NFW}}$  to the superfluid density  $\rho_{\text{SF}}$  at a radius  $r_{\text{NFW}}$  that is chosen to maximize  $M_{200}^{\text{DM}}$ . This gives the most conservative upper bound for  $M_{200}^{\text{DM}}$ . We restrict  $r_{\text{NFW}}$  only in two ways. First, we assume a positive superfluid energy density within the superfluid core which implies that  $r_{\text{NFW}}$  is smaller than the radius  $r_m$  where  $\rho_{\text{SF}}$  vanishes. Second, we assume all rotation curve data points to be within the superfluid core. Thus, we also restrict  $r_{\text{NFW}}$  to be larger than  $R_{\text{max}}$ . This is illustrated in Fig. D.9.

To get the largest possible  $M_{200}^{\text{DM}}$  compatible with our constraints, we can now scan values of  $\varepsilon$  in  $(\varepsilon_{\text{min}}, 0.4)$  and values of  $r_{\text{NFW}}$  in  $(R_{\text{max}}, r_m)$  and record the largest  $M_{200}^{\text{DM}}$  as an upper bound  $M_{200}^{\text{DM,max}}$ . For a given  $\varepsilon$  and  $r_{\text{NFW}}$  we calculate  $M_{200}^{\text{DM}}$  by solving the equation

$$\frac{4\pi}{3}\rho_{200}r_{200}^3 = M_{\text{SF}}(r_{\text{NFW}}) + 4\pi r_{\text{NFW}}^3 \rho_{\text{SF}}(r_{\text{NFW}}) \ln\left(\frac{r_{200}}{r_{\text{NFW}}}\right) \quad (\text{D.4})$$

for  $r_{200}$  and then plugging the result into  $M_{200}^{\text{DM}} = (4\pi/3)\rho_{200}r_{200}^3$ . We calculate  $M_{\text{SF}}(r)$  as  $-(\hat{\mu}'_{\text{SF}}(r)/m)(r^2/G)$ . For some galaxies, it is not possible to solve the  $\hat{\mu}_{\text{SF}}$  equation with  $|\varepsilon| < 0.4$ , if we require a positive  $\rho_{\text{SF}}$  up to the last rotation curve data point. Such galaxies are excluded in the results shown below.

For the baryonic mass distribution we use the same values  $(M/L_*)_{\text{disk}} = 0.5$  and  $(M/L_*)_{\text{bulge}} = 0.7$  for all galaxies. These may not give the best fit to the measured rotation curves for all

galaxies. However, here we are not interested in the fit to the rotation curve data, but in whether or not it is possible to have, at the same time, both a rotation curve in the proper MOND limit and sufficient  $M_{200}^{\text{DM}}$  for strong lensing. The precise value of  $M/L_*$  is irrelevant for this.

We can simplify the scanning procedure a bit. Namely, Fig. D.12 and Fig. D.13 suggest that increasing the boundary condition  $\varepsilon \equiv \varepsilon_*(R_{\text{mid}})$  increases  $\varepsilon_*(r)$  at all radii, not just at  $R_{\text{mid}}$ . We have verified this numerically for various galaxies and boundary conditions. Here, we assume that this is true in general.<sup>2</sup> Consequences of this are that a larger boundary condition  $\varepsilon$  implies an everywhere larger superfluid energy density and a larger radius  $r_m$  where this energy density reaches zero. Therefore, for a fixed  $r_{\text{NFW}}$ , the quantity  $M_{200}^{\text{DM}}$  is a monotonically increasing function of  $\varepsilon$ . Thus, we can simplify our scanning procedure by always setting  $\varepsilon = 0.4$  and scanning only values of  $r_{\text{NFW}}$  in  $(R_{\text{max}}, r_m)$ . For this, we use Mathematica's 'NMaximize' function with its default options.

It can happen that the NFW radius  $r_{\text{NFW}}$  is bigger than the radius  $r_{\infty}$  up to which we numerically solved for  $\hat{\mu}_b$  (usually 100 kpc, see Appendix C.1). In this case, we must continue  $\hat{\mu}_b$  beyond  $r_{\infty}$  since solving the  $\hat{\mu}_{\text{SF}}$  equation requires  $\hat{\mu}_b$  and  $a_b$  up to  $r_{\text{NFW}}$ . For simplicity, we continue  $\hat{\mu}_b$  beyond  $r_{\infty}$  assuming spherical symmetry and zero baryonic energy density at  $r > r_{\infty}$ ,

$$\frac{\hat{\mu}_b(r > r_{\infty})}{m} = \frac{\hat{\mu}(r_{\infty})}{m} - a_{b,R}(r_{\infty})r_{\infty}^2 \left(\frac{1}{r_{\infty}} - \frac{1}{r}\right). \quad (\text{D.5})$$

This implies  $a_b(r > r_{\infty}) = a_{b,R}(r_{\infty})r_{\infty}^2/r^2$ . We expect errors due to this to not significantly change our results.

Below we need the total baryonic mass  $M_b$  of each galaxy. We adopt

$$M_b \equiv 0.5 \cdot (L_{[3.6]} - L_{\text{bulge}}) + 0.7 \cdot L_{\text{bulge}} + 1.4 \cdot M_{\text{HI}}, \quad (\text{D.6})$$

where  $L_{[3.6]}$ ,  $L_{\text{bulge}}$ , and  $M_{\text{HI}}$  are taken directly from SPARC. They denote the total [3.6] luminosity, the total bulge luminosity, and the HI mass, respectively. The stellar luminosities are weighted by their respective mass-to-light ratio. The factor 1.4 in front of the HI mass is to take into account helium and molecular hydrogen (McGaugh et al. 2020).

We show the results in Fig. 6. We see that large ratios  $M_{200}^{\text{DM}}/M_b$  are easier to reach for galaxies with relatively small baryonic masses  $M_b$ . In part, this is due to the factor  $1/M_b$  in  $M_{200}^{\text{DM}}/M_b$ . For strong lensing, relatively large baryonic masses are relevant. To illustrate this, we also show the best-fit values from the SFDM strong lensing analysis from Hossenfelder & Mistele (2019) in Fig. 6. These lensing galaxies tend to have  $M_b \gtrsim 10^{11} M_{\odot}$  and  $M_{200}^{\text{DM}}/M_b \gtrsim 1000$ . In contrast, the SPARC galaxies with  $M_b > 10^{11} M_{\odot}$  almost all have  $M_{200}^{\text{DM}}/M_b < 10$  when restricted to have rotation curves in the MOND limit, i.e. when restricted to  $|\varepsilon| < 0.4$ . This is a stark contrast. The SPARC galaxies don't reach baryonic masses quite as large as the lensing galaxies from Hossenfelder & Mistele (2019). But from Fig. 6, it seems clear that the trend goes into the wrong direction: The

<sup>2</sup> Indeed, a violation of this would imply that the boundary value problem is non-unique, contrary to what we already implicitly assumed in our calculations above, where we assumed that a value  $\varepsilon_*(R_{\text{mid}})$  uniquely specifies a solution. The reason is the following. If a larger boundary condition  $\varepsilon_*(R_{\text{mid}})$  gives a smaller  $\varepsilon_*(r)$  at some radius  $r = r_l$ , then by continuity there must be a radius  $r_x$  between  $R_{\text{mid}}$  and  $r_l$  where the solutions  $\varepsilon_*(r)$  for two different boundary conditions have the same value. Thus, the boundary value problem with boundary conditions imposed at  $r = r_x$  is non-unique.

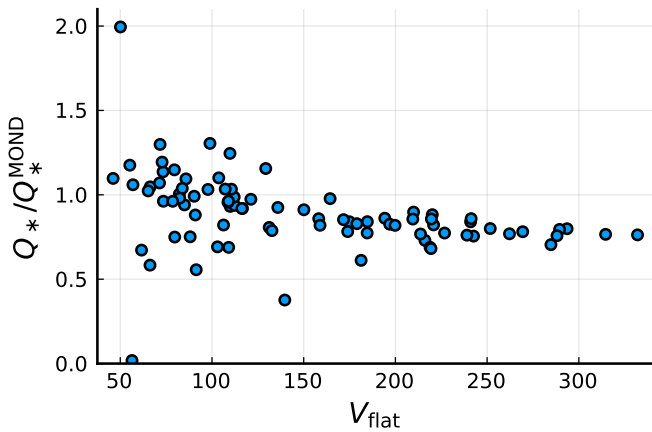


Fig. D.10. Same as Fig. 5 but for two-field SFDM.

larger the galaxy, the smaller the ratio  $M_{200,\text{max}}^{\text{DM}}/M_b$  (assuming  $|\varepsilon| < 0.4$ ).

Thus, it seems that a rotation curve in the MOND limit and sufficient dark matter for strong lensing are indeed mutually exclusive in standard SFDM. A caveat is that the galaxies in the SPARC sample are not ellipticals, in contrast to the lensing sample used in Hossenfelder & Mistele (2019). One might think that, for a given  $M_b$ , the maximum possible  $M_{200}^{\text{DM}}$  is not sensitive to the details of the baryonic mass distribution since the main contributions to  $M_{200}^{\text{DM}}$  come from large radii where, to a first approximation, only the total  $M_b$  plays a role. However, we impose the condition  $|\varepsilon| < 0.4$  at relatively small radii  $R = R_{\text{mid}}$  where the details of the baryonic mass distribution may still matter. Indeed, the sensitivity of  $M_{200,\text{max}}^{\text{DM}}$  to these details is reflected in the scatter in Fig. 6 (see also the end of Appendix D.5). Still, even being generous with this scatter, it seems unlikely that the difference in galaxy type explains why the SPARC galaxies restricted to  $|\varepsilon| < 0.4$  cannot reach larger values of  $M_{200}^{\text{DM}}/M_b$ . Also, Fig. 6 suggests that for  $M_{200}^{\text{DM}}/M_b$  values closer to those required for strong lensing (when restricting to  $|\varepsilon| < 5$  instead of  $|\varepsilon| < 0.4$ ) there is less scatter, i.e. less sensitivity to the baryonic mass distribution beyond the total  $M_b$ .

This suggests that strong lensing galaxies cannot have their inner parts (where rotation curves or velocity dispersions are measured) be in the proper MOND limit  $|\varepsilon_*| \ll 1$ . This is not in direct contradiction with measurements. Indeed, Hossenfelder & Mistele (2019) successfully fitted strong lensing data in SFDM. But one cannot easily keep the key idea of SFDM that the inner parts of galaxies are always in the proper MOND limit. Either one has to give up this key idea or one has to postulate that it does not apply to strong lensing galaxies for some reason.

#### D.4. $M/L_*$ in two-field SFDM

By construction, the phonon acceleration in two-field SFDM should almost always be close to  $\sqrt{a_0 a_b}$  (Mistele 2021). The superfluid’s Newtonian gravitational pull can be comparable to that of standard SFDM (Mistele 2021). Thus, we expect the fit results for two-field SFDM to be close to that of the ‘SFDM  $a_\theta = \sqrt{a_0 a_b}$ ’ model discussed above.

This should be true at least for the stellar mass-to-light ratios and the best-fit  $\chi^2$ . The results for  $f_{\text{DM}}$  may be not as close since the superfluid halo’s shape is different. We will discuss the superfluid halo in more detail below.

As expected, the best fits for two-field SFDM are almost all in the  $|\varepsilon_*| \ll 1$  limit so that their phonon force  $a_\theta$  is close to  $\sqrt{a_0 a_b}$ . This is shown in Fig. D.4. Only for two galaxies (NGC6789, UGC07232) does  $\varepsilon_*$  become larger than 0.1. Its largest values is 0.36 for NGC6789.

The averaged best-fit stellar mass-to-light ratios and the best-fit  $\chi^2$  can be found in Table D.1, Table D.2, and Fig. D.11. As expected, these are almost identical to those of the ‘SFDM  $a_\theta = \sqrt{a_0 a_b}$ ’ model discussed above.

Two-field SFDM gives a systematically smaller  $M/L_*$  than MOND only for high-acceleration galaxies, not for low-accelerations, just as standard SFDM (see Appendix D.2.4). See Fig. D.10 for an example.

##### D.4.1. The minimum acceleration

In two-field SFDM, the equilibrium on galactic scales is stable only for phonon accelerations above a certain minimum acceleration. This minimum acceleration depends on the value of the field  $\hat{\mu}/m$ . Assuming  $|\varepsilon_*| \ll 1$ , as is usually the case, stability requires

$$a_b \left( 10^7 \frac{\hat{\mu}}{m} \right)^2 > \bar{a}, \quad (\text{D.7})$$

where  $\bar{a}$  is one of this model’s parameters. Often,  $\hat{\mu}/m$  is on the order of  $10^{-7}$  on galactic scales. Thus, roughly, stability requires

$$a_b \gtrsim \bar{a}. \quad (\text{D.8})$$

When  $\hat{\mu}/m$  is smaller, the instability sets in earlier. Mistele (2021) chose  $\bar{a} = 10^{-12} \text{ m/s}^2$  so that this model does not predict standard MOND-like behavior for dwarf spheroidals that may start to deviate from MOND-like behavior around  $a_b \sim 10^{-12} \text{ m/s}^2$  (Lelli et al. 2016). In our two-field SFDM fit we adopt this value of  $\bar{a}$ .

For galaxies violating Eq. (D.7), we should in principle model what happens beyond the minimum acceleration in two-field SFDM. Here, we will not do this for two reasons. First, this regime is not well-understood. Second, we are interested in the MOND regime inside the superfluid core. Modelling the behavior beyond the minimum acceleration will not help us understand whether or not the MOND regime of two-field SFDM requires a larger or smaller  $M/L_*$  than standard MOND models.

Still, 98 of 169 SPARC galaxies violate the condition Eq. (D.7) at  $R_{\text{max}}$ . For these galaxies, our fit is not meaningful since it relies on an unstable equilibrium. This is expected for the dwarf spheroidals with  $a_b$  around  $10^{-12} \text{ m/s}^2$ . But the 98 galaxies violating Eq. (D.7) include many more galaxies, also at  $a_b \gg \bar{a}$ . We will have to deal with this one way or another.

To further explore this, we have redone the two-field SFDM fit with the much smaller value  $\bar{a} = 10^{-14} \text{ m/s}^2$ . This is listed as ‘two-field  $a_{\text{min}}^{\text{small}}$ ’ in our tables and figures. The resulting  $M/L_*$  and  $\chi^2$  values are almost identical to those of the previous two-field SFDM fit. But still 71 galaxies violate Eq. (D.7).

Thus, Eq. (D.7) is often not violated because  $a_b$  is smaller than  $\bar{a}$  but because  $\hat{\mu}/m$  is smaller than  $10^{-7}$ . A small  $\hat{\mu}/m$  corresponds to a small superfluid mass  $M_{\text{DM}}$ . Indeed, Fig. D.3 shows that many galaxies have a smaller  $f_{\text{DM}}$  in two-field SFDM compared to standard SFDM, for both  $\bar{a}$  values discussed above.

This raises two questions. First, does two-field SFDM really need to go to small  $\hat{\mu}/m$  to fit the SPARC data, thus often violating Eq. (D.7)? Second, why does standard SFDM tend to end up at larger  $f_{\text{DM}}$  values than two-field SFDM?

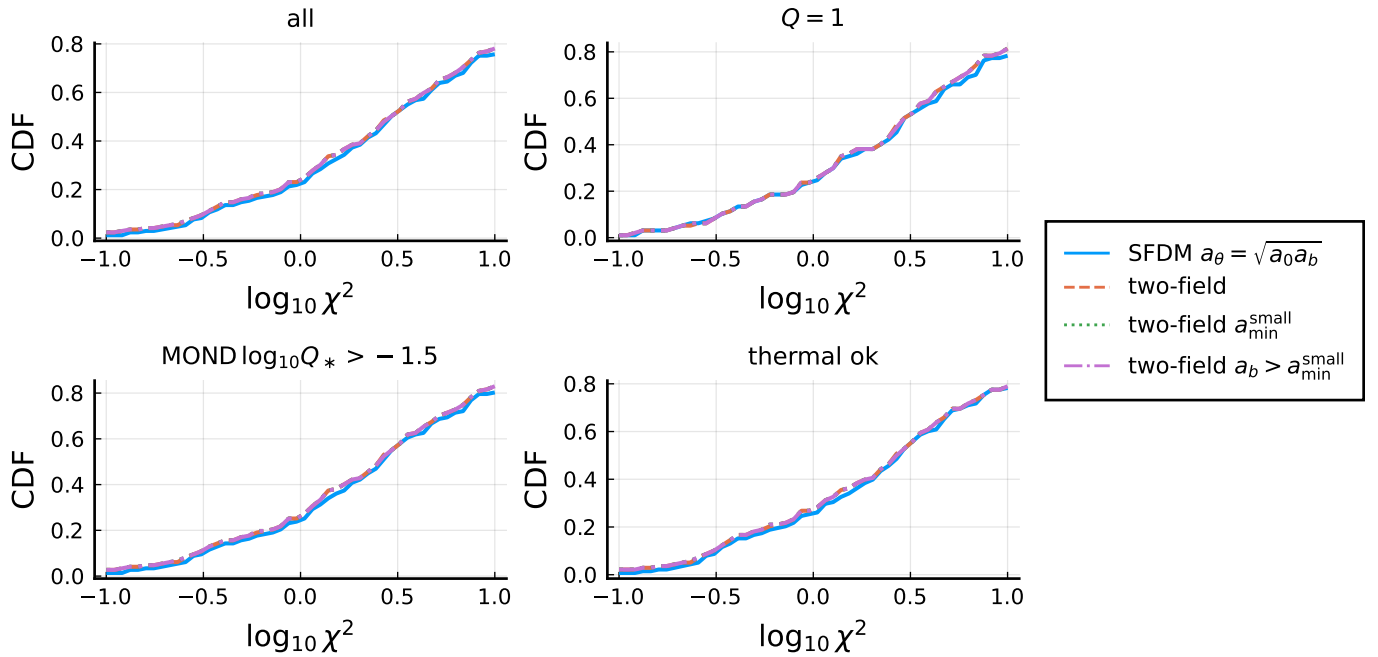


**Fig. D.11.** The  $\chi^2$  CDFs for the different two-field models and galaxy cuts. Also shown is the ‘SFDM  $a_\theta = \sqrt{a_0 a_b}$ ’ fit for comparison.

#### D.4.2. Origin of the small $f_{M_{\text{DM}}}$ values in two-field SFDM

The best-fit  $\chi^2$  and  $M/L_*$  are almost identical for the two-field SFDM fits and for the standard SFDM fit with  $a_\theta = \sqrt{a_0 a_b}$ . But the superfluid halos of two-field SFDM reach much smaller masses than those in standard SFDM (see Fig. D.3). For example, there are no galaxies at  $f_{M_{\text{DM}}} < -2.3$  in any standard SFDM fit, but many such galaxies in two-field SFDM. The only relevant difference between two-field SFDM and the ‘SFDM  $a_\theta = \sqrt{a_0 a_b}$ ’ model is the difference in their  $\rho_{\text{SF}}$ . Thus, this different superfluid energy density must be the reason for the qualitative difference in  $f_{M_{\text{DM}}}$ . Here, we explain this in more detail.

As discussed above, we enforce a positive superfluid energy density at radii smaller than the last rotation curve data point, i.e.  $\rho_{\text{SF}} > 0$  at  $R \leq R_{\text{max}}$ . The difference between standard and two-field SFDM regarding small dark matter masses boils down to what this condition implies.

Consider first two-field SFDM. In two-field SFDM, the superfluid energy density vanishes when  $\hat{\mu}/m = 0$ . Equivalently, when  $\varepsilon_* = 0$ . Typically,  $\hat{\mu}/m$  is a decreasing function of galactocentric radius.<sup>3</sup> Thus, whenever the condition  $\rho_{\text{SF}} > 0$  is fulfilled at the largest radius of interest,  $R = R_{\text{max}}$ , it is fulfilled at all radii of interest, i.e. at  $R \leq R_{\text{max}}$ . In a given galaxy, a smaller superfluid mass  $M_{\text{SF}}(R)$  at some radius, e.g. at  $R = R_{\text{max}}$ , implies a smaller  $\hat{\mu}/m$  everywhere in the superfluid core (not just at  $R = R_{\text{max}}$ ). Indeed, different superfluid masses just correspond to adding a term  $\sin(r/r_0)/r$  with a different prefactor to  $\hat{\mu}_{\text{SF}}$ , see Appendix C.4. Thus, if we go to smaller and smaller  $f_{M_{\text{DM}}}$ , we go to smaller and smaller  $\hat{\mu}/m$ . At some point,  $\hat{\mu}/m$  will become negative at  $R = R_{\text{max}}$ . Then, we are at the minimum possible  $f_{M_{\text{DM}}}$  allowed by our condition  $\rho_{\text{SF}} > 0$ .

<sup>3</sup> This is always the case in spherical symmetry as long as  $\rho_{\text{SF}}$  is positive. Indeed, then  $\hat{\mu}'(r)/m = -G(M_b + M_{\text{SF}})/r^2 < 0$ . Here, we assume spherical symmetry only for  $\hat{\mu}_{\text{SF}}$ , but not for  $\hat{\mu}_b$ . Thus, only  $\hat{\mu}_{\text{SF}}$  is guaranteed to be a decreasing function of galactocentric radius, not the total  $\hat{\mu}$ . Still, the total  $\hat{\mu}(R, z = 0)$  typically decreases as a function of  $R$  also in our case.

The condition  $\rho_{\text{SF}} > 0$  at  $R = R_{\text{max}}$  enforces a minimum possible mass also in standard SFDM. A difference is that the superfluid energy density in standard SFDM vanishes not at  $\varepsilon_* = 0$  but at a negative value  $\varepsilon_{*\text{min}} \approx -0.31$  (for  $\beta = 2$ ). Using the definition of  $\varepsilon_*$  from Eq. (1), this constant negative lower bound on  $\varepsilon_*(\mathbf{x})$  becomes a non-constant lower bound  $\hat{\mu}_{\text{min}}(\mathbf{x})$  on  $\hat{\mu}(\mathbf{x})$ . This is illustrated in Fig. D.12 for NGC2403. The top panel shows solutions  $\hat{\mu}/m$  for various boundary conditions  $\varepsilon$ . The bottom panel shows  $\varepsilon_*$  for the same boundary conditions. Both panels also show the lower bounds on  $\varepsilon_*$  and  $\hat{\mu}$ , respectively, which ensure  $\rho_{\text{SF}} > 0$ . For the smallest boundary condition value  $\varepsilon = 0.08$  shown in Fig. D.12, both  $\varepsilon_*$  and  $\hat{\mu}$  reach this lower bound at  $R = R_{\text{max}}$ . Thus,  $\varepsilon = 0.08$  corresponds to the smallest possible superfluid mass that is allowed by the condition  $\rho_{\text{SF}} > 0$ . Lower superfluid masses require reaching  $\rho_{\text{SF}} = 0$  before  $R = R_{\text{max}}$  which we do not allow. This is similar as in two-field SFDM.

However, in contrast to two-field SFDM, this constraint at  $R = R_{\text{max}}$  is not the only constraint on superfluid masses in standard SFDM. In standard SFDM, having  $\rho_{\text{SF}} > 0$  at  $R = R_{\text{max}}$  does not imply  $\rho_{\text{SF}} > 0$  at smaller radii. The main issue is at  $R = 0$ . This is illustrated in Fig. D.13 for DDO168. For the smallest boundary condition value  $\varepsilon = -0.06$  shown in Fig. D.13, at  $R = R_{\text{max}}$ , both  $\hat{\mu}/m$  and  $\varepsilon_*$  are not close to the minimum values that  $\rho_{\text{SF}} > 0$  allows. However, at  $R = 0$ , the minimum values are reached, i.e.  $\rho_{\text{SF}}$  vanishes. Thus, the boundary condition  $\varepsilon = -0.06$  corresponds to the minimum possible  $f_{M_{\text{DM}}}$  allowed by our condition  $\rho_{\text{SF}} > 0$ . But now the constraint comes from  $R = 0$  rather than  $R = R_{\text{max}}$ .

To understand this, consider small radii,  $R \rightarrow 0$ . At  $R \rightarrow 0$ , the field  $\hat{\mu}$  reaches a finite value  $\hat{\mu}(0)$ . The Newtonian baryonic acceleration  $|\mathbf{a}_b(R)|$  goes to zero, typically  $a_b \propto R$  for  $R \rightarrow 0$ . Thus, we have from the definition of  $\varepsilon_*$  Eq. (1)

$$\varepsilon_*(R \rightarrow 0) \propto \frac{\hat{\mu}(0)}{R} \rightarrow \pm\infty. \quad (\text{D.9})$$

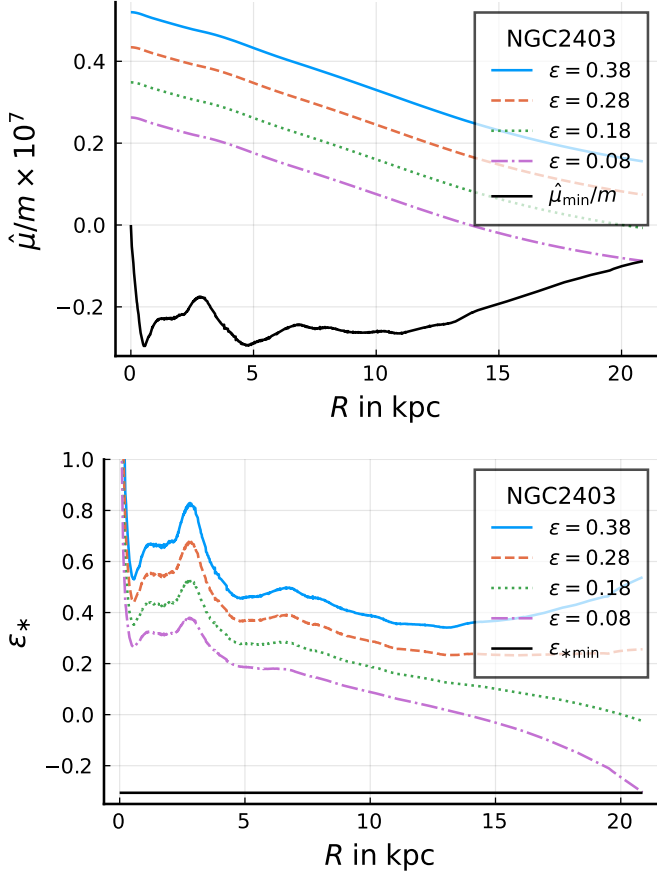


**Fig. D.12.** Top: The quantity  $\hat{\mu}/m$  at  $z = 0$  for various boundary conditions  $\varepsilon$  for the galaxy NGC2403 assuming the best-fit  $Q_*$  for SFDM. The solid black line shows the minimum possible value of  $\hat{\mu}/m$  allowed by the condition  $\rho_{\text{SF}} > 0$  at each radius. The smallest boundary condition  $\varepsilon = 0.08$  corresponds to the minimum possible dark matter mass for the given baryonic mass distribution. Smaller masses would require that the condition  $\rho_{\text{SF}} > 0$  is violated before  $R = R_{\text{max}}$ . Bottom: Same as the top panel but showing  $\varepsilon_*$  instead of  $\hat{\mu}/m$ . The minimum possible  $\varepsilon_*$  allowed by  $\rho_{\text{SF}} > 0$  is a constant.

That is,  $\varepsilon_*$  tends to  $\pm\infty$  with the sign being that of  $\hat{\mu}(0)$ . A positive  $\rho_{\text{SF}}$  requires  $\varepsilon_*(0) \geq \varepsilon_{*\text{min}}$ . Thus, we must have

$$\hat{\mu}(0) \geq 0. \quad (\text{D.10})$$

This condition  $\hat{\mu}(0) > 0$  must also hold in two-field SFDM. But, in two-field SFDM,  $\hat{\mu}(0) > 0$  follows from  $\rho_{\text{SF}} > 0$  at  $R = R_{\text{max}}$ . This is because  $\hat{\mu}$  is a decreasing function of radius and because  $\rho_{\text{SF}} > 0$  requires  $\hat{\mu} > 0$  even at  $R = R_{\text{max}}$ . So this adds nothing in two-field SFDM.

This is different in standard SFDM. A positive  $\rho_{\text{SF}}$  at  $R = R_{\text{max}}$  does not necessarily imply a positive  $\hat{\mu}(0)$  and thus a positive  $\rho_{\text{SF}}$  at  $R = 0$ . Since  $\hat{\mu}$  is a decreasing function of radius, violating  $\hat{\mu}(0) > 0$  is possible only if  $\hat{\mu}$  is negative already at  $R = R_{\text{max}}$ . Consider this case where  $\hat{\mu}$  is negative at  $R = R_{\text{max}}$ . Since  $\hat{\mu}$  decreases with radius, it can happen that  $\hat{\mu}$  grows sufficiently between  $R = R_{\text{max}}$  and  $R = 0$  to become positive at  $R = 0$ . In this case the condition  $\hat{\mu}(0) > 0$ , corresponding to  $\rho_{\text{SF}} > 0$  at  $R = 0$ , gives no additional constraint. However, this is not guaranteed to happen. When  $\hat{\mu}$  does not grow sufficiently, the condition  $\hat{\mu}(0) > 0$  gives an additional constraint. This is what happens for DDO168 as illustrated in Fig. D.13.

This, then, is the reason why two-field SFDM allows smaller superfluid masses, i.e. smaller  $f_{\text{MDM}}$ , compared to standard

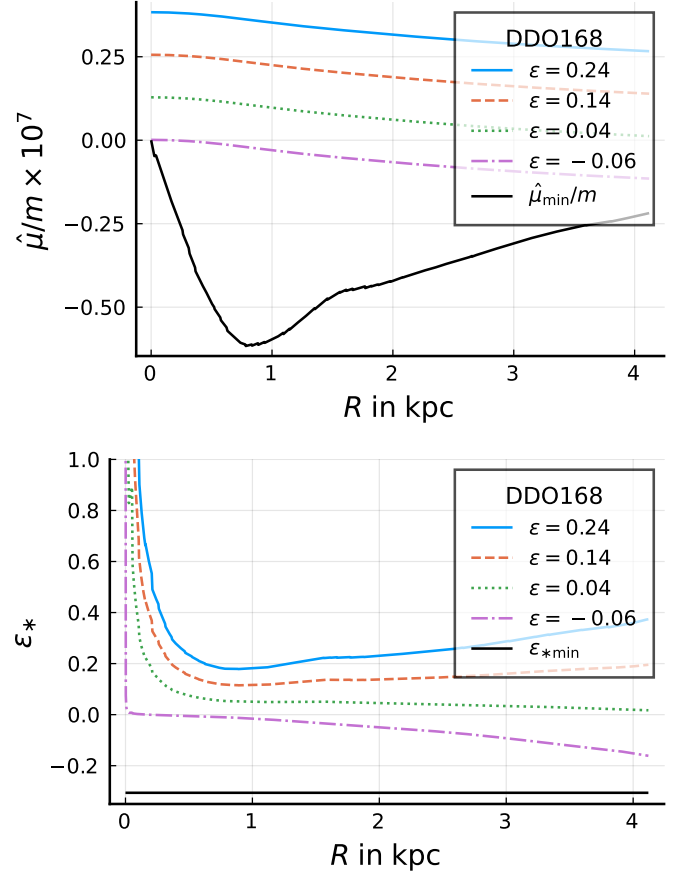


**Fig. D.13.** Top: Same as Fig. D.12, top, but for DDO168. The smallest boundary condition  $\varepsilon = -0.06$  shown again corresponds to the minimum possible mass allowed by  $\rho_{\text{SF}} > 0$ . But now smaller masses would violate this condition at  $R = 0$  instead of at  $R = R_{\text{max}}$ . Bottom: Same as Fig. D.12, bottom, but for DDO168.

SFDM. In both models, small superfluid masses correspond to  $\rho_{\text{SF}}$  close to zero. And in both cases one needs to be careful not to let this density become negative (or ill-defined) at  $R = R_{\text{max}}$ . However, in standard SFDM, being close to  $\rho_{\text{SF}} = 0$  implies a negative  $\hat{\mu}$ , and in this case there can be an additional constraint at  $R = 0$ , as just discussed. This second constraint is absent in two-field SFDM where  $\rho_{\text{SF}}$  vanishes already at  $\hat{\mu} = 0$ .

As mentioned above, this second constraint in standard SFDM occurs only when  $\hat{\mu}$  does not grow sufficiently between  $R = R_{\text{max}}$  and  $R = 0$ . We will now make this more precise. The minimum allowed superfluid mass from the constraint at  $R = R_{\text{max}}$  corresponds to  $\rho_{\text{SF}} = 0$  at  $R = R_{\text{max}}$ . This constraint is present in both standard and two-field SFDM. Reaching this minimum mass implies

$$\hat{\mu}(R_{\text{max}}) = \varepsilon_{*\text{min}} \frac{\alpha M_{\text{Pl}} |a_b(R_{\text{max}})|}{2m}. \quad (\text{D.11})$$

A second constraint  $\hat{\mu}(0) > 0$  from  $R = 0$  is avoided whenever  $\hat{\mu}$  grows between  $R = R_{\text{max}}$  and  $R = 0$  by at least

$$\hat{\mu}(0) - \hat{\mu}(R_{\text{max}}) > -\varepsilon_{*\text{min}} \frac{\alpha M_{\text{Pl}} |a_b(R_{\text{max}})|}{2m}. \quad (\text{D.12})$$

As the example of DDO168 (see Fig. D.13) shows, this is not always guaranteed in standard SFDM. But in some cases it is. Namely, as in Appendix C.2, we can write  $\hat{\mu} = \hat{\mu}_b + \hat{\mu}_{\text{SF}}$ . Both  $\hat{\mu}_b$  and  $\hat{\mu}_{\text{SF}}$  typically decrease with radius, with the amount they



decrease being determined by the baryonic and superfluid mass, respectively. Once we know the baryonic mass distribution, we know a lower bound on how much the total  $\hat{\mu}$  grows, independently of the superfluid energy density and the boundary condition  $\varepsilon$ . As a result, if the baryonic mass alone makes  $\hat{\mu}$  grow sufficiently, we never get an additional constraint from  $\hat{\mu}(0) > 0$ . This is the case if

$$\hat{\mu}_b(0) - \hat{\mu}_b(R_{\max}) > -\varepsilon_{*\min} \frac{\alpha M_{\text{Pl}} |a_b(R_{\max})|}{2m}. \quad (\text{D.13})$$

Thus, more quantitatively, we claim that standard SFDM cannot get masses as low as two-field SFDM because Eq. (D.13) is often not satisfied so that there is an additional constraint from  $R = 0$  in standard SFDM which is not present in two-field SFDM. We expect that, without this constraint, galaxies would end up at smaller  $f_{M_{\text{DM}}}$  also in standard SFDM.

As a consequence, we expect that the galaxies that end up at very small  $f_{M_{\text{DM}}}$  in two-field SFDM but not in standard SFDM violate Eq. (D.13). To check this, we have selected the 30 galaxies that have  $f_{M_{\text{DM}}} < -2.3$  in two-field SFDM. As mentioned above, no galaxies have such small  $f_{M_{\text{DM}}}$  in standard SFDM. For the most direct comparison against two-field SFDM we use the best-fit stellar  $M/L_*$  from the 'SFDM  $a_\theta = \sqrt{a_0 a_b}$ ' fits. We find that these 30 galaxies all violate Eq. (D.13) so that they face an additional constraint in standard SFDM. This confirms our explanation why galaxies reach smaller  $f_{M_{\text{DM}}}$  values in two-field SFDM compared to standard SFDM.

#### D.4.3. Enforcing the minimum acceleration in two-field SFDM

In Appendix D.4.1, we saw that many best-fits in two-field SFDM violate the minimum acceleration condition Eq. (D.7), even with a reduced  $\bar{a}$  value. The reason is that many galaxies end up at small  $\hat{\mu}/m$ , or, equivalently, at small superfluid masses corresponding to small  $f_{M_{\text{DM}}}$  (see Appendix D.4.2).

For small superfluid masses, the precise mass is often not important for fitting rotation curves since the corresponding  $a_{\text{SF}}$  is subdominant. Thus, it may be possible that we can find fits with sufficiently large  $\hat{\mu}/m$  so that all galaxies satisfy the minimum acceleration condition without getting significantly worse fits. To check this, we have redone the two-field SFDM fit with  $\bar{a} = 10^{-14} \text{ m/s}^2$  but with the the minimum acceleration condition Eq. (D.7) enforced. That is, whenever this condition is violated we set  $\chi^2 = 10^{10}$  so that our fit code goes elsewhere. We label this model as 'two-field  $a_b > a_{\min}^{\text{small}}$ '.

As we can see from Table D.1, Table D.2, and Fig. D.11, this gives almost identical results for the best-fit  $\chi^2$  and  $M/L_*$  values as the previous two-field SFDM fits. This shows that it is not necessary for two-field SFDM to violate the minimum acceleration condition. The small  $\hat{\mu}/m$  values are not required to get a reasonable fit, see also Fig. D.3.

#### D.5. Tension with strong-lensing in two-field SFDM

In two-field SFDM, the  $|\varepsilon_*| \ll 1$  condition is almost always fulfilled so that the phonon force is almost always close to the MOND-like value  $\sqrt{a_0 a_b}$ . So, in contrast to standard SFDM, simultaneously being in the  $|\varepsilon_*| \ll 1$  limit and producing a sufficient strong lensing signal is not a problem. However, in two-field SFDM, a small  $\varepsilon_*$  does not imply that  $a_{\text{SF}}$  is negligible. So two-field SFDM may still not be able to have naturally MOND-like rotation curves and a sufficient strong lensing signal at the same time.

To check this, we calculate a maximum total dark matter mass  $M_{200}^{\text{DM}}$  in the same way as we did for standard SFDM in Appendix D.3. But instead of imposing  $|\varepsilon| < 0.4$  we impose

$$a_{\text{SF}} < 0.3 (a_b + a_\theta), \quad (\text{D.14})$$

at  $R = R_{\max}$ . For simplicity, we assume  $a_\theta = \sqrt{a_0 a_b}$  which is usually a good approximation. Then, Eq. (D.14) becomes

$$\frac{GM_{\text{DM}}(R_{\max})}{R_{\max}^2} < 0.3 \cdot (a_b + \sqrt{a_0 a_b}). \quad (\text{D.15})$$

Here, we use  $M_{\text{DM}}(R_{\max})$  instead of  $\varepsilon_*(R_{\text{mid}})$  as a boundary condition. This gives a condition on  $\hat{\mu}'_{\text{SF}}(R_{\max})/m$  instead of on  $\hat{\mu}(R_{\text{mid}})/m$ . We can still solve the two-field equations as described in Appendix C.4 with this modified boundary condition.

The value 0.3 is somewhat arbitrary. It is chosen to give a non-negligible but still sub-dominant  $a_{\text{SF}}$ . There is a clear trade-off here. Larger values allow for larger total dark matter masses  $M_{200}^{\text{DM}}$  but also larger deviations from naturally MOND-like rotation curves. Smaller values give more naturally MOND-like rotation curves but also smaller total dark matter masses.

One way to find the largest possible  $M_{200}^{\text{DM}}$  compatible with the condition Eq. (D.15) is to just scan over all possible  $M_{\text{DM}}(R_{\max})$  satisfying the condition. But we don't have to do this here for the same reason we didn't have to do it for standard SFDM, see Appendix D.3. Basically, since a larger  $M_{\text{DM}}(R_{\max})$  always gives a larger  $M_{200}^{\text{DM}}$ .

Above, we considered different values of the parameter  $\bar{a}$  which determines the minimum acceleration. Here, we use  $\bar{a} = 10^{-12} \text{ m/s}^2$ . But the choice of  $\bar{a}$  does not actually affect the maximum  $M_{200}^{\text{DM}}$  we calculate since we keep  $r_0$  and  $a_0$  fixed. It only determines how small  $\varepsilon_*$  is since  $m^2/\alpha \propto (\bar{a}/a_0)^{1/4}$ . That is, it determines how good our approximation  $a_\theta = \sqrt{a_0 a_b}$  works. Since, by construction,  $|\varepsilon_*| \ll 1$  for any reasonable value of  $\bar{a}$ , this approximation works well for any reasonable  $\bar{a}$ .

The result is shown in Fig. 9 and discussed in Sec. 5.3.

Comparing Fig. 9 for two-field SFDM and Fig. 6 for standard SFDM, there is less scatter in the derived relation between  $M_{200, \max}^{\text{DM}}$  and  $M_b$  for two-field SFDM. This is likely because this relation in two-field SFDM is less sensitive to the details of the baryonic mass distribution at a given total baryonic mass  $M_b$ . There are a few reasons for this. First, the superfluid energy density  $\rho_{\text{SF}}$  scales as  $\sqrt{a_b}$  in standard SFDM (at least in the MOND limit  $|\varepsilon_*| \ll 1$ ) but not in two-field SFDM. Second, we impose the condition  $|\varepsilon| < 0.4$  in standard SFDM at smaller radii  $R = R_{\text{mid}}$  than  $a_{\text{SF}}/(a_b + a_\theta) < 0.3$  in two-field SFDM which we impose at  $R = R_{\max}$ . There is less variation in the baryonic mass distribution at larger radii. Third, these conditions depend on different quantities. The left-hand side of  $|\varepsilon| < 0.4$  in standard SFDM scales as  $\hat{\mu}/a_b$  while the left-hand side of  $a_{\text{SF}}/(a_b + a_\theta) < 0.3$  in two-field SFDM scales as  $M_{\text{SF}}/\sqrt{a_b}$ , at least at larger radii where  $a_\theta \propto \sqrt{a_b}$  dominates. The acceleration  $a_{\text{SF}}$  depends only on  $\hat{\mu}_{\text{SF}}$  while  $\hat{\mu}$  also depends on  $\hat{\mu}_b$  which is much more sensitive to the details of the baryonic mass distribution. Similarly,  $\sqrt{a_b}$  is less sensitive to these details than  $a_b$ .